Solar Phys (2018) 293:166
https://doi.org/10.1007/s11207-018-1384-4

Physical Processes Involved in the EUV "Surge" Event of 9 May 2012

Marcelo López Fuentes[1] · Cristina H. Mandrini[1,2] · Mariano Poisson[1] · Pascal Démoulin[3] · Germán Cristiani[1,2] · Fernando M. López[4] · Maria Luisa Luoni[1]

Received: 30 April 2018 / Accepted: 24 November 2018

Abstract We study an extreme ultraviolet (EUV) confined ejection observed on 9 May 2012 in Active Region (AR) NOAA 11476. For the analysis we use observations in multiple wavelengths (EUV, X-rays, Hα, and magnetograms) from a variety of ground- and space-based instruments. The magnetic configuration showed two rotating bipoles within the following polarity of the AR. This evolution was present some tens of hours before the studied event and continued thereafter. During this period, the magnetic flux of both bipoles continuously decreased. A mini-filament with a length of $\approx 30''$ lay along the photospheric inversion line of the largest bipole. The mini-filament was observed to erupt, accompanied by an M4.7 flare (SOL20120509T12:23:00). This injected dense material as well as twist along closed loops in the form of a very broad ejection whose morphology resembled that of typical Hα surges. We conclude that the flare and eruption can be explained as due to two reconnection processes, one occurring below the erupting mini-filament, and another above it. This second process injects the mini-filament plasma within the reconnected closed loops linking the main AR polarities. By analyzing the magnetic topology using a force-free model of the coronal field, we identify the location of quasi-separatix layers, where reconnection is prone to occur, and present a detailed interpretation of the chromospheric and coronal eruption observations. In particular, this event, in contrast to what has been proposed in several models explaining surges and/or jets, is not produced by magnetic flux emergence, but by magnetic flux cancellation accompanied by the rotation of the bipoles. In fact, the conjunction of these

Electronic supplementary material The online version of this article (https://doi.org/10.1007/s11207-018-1384-4) contains supplementary material, which is available to authorized users.

✉ M. López Fuentes
lopezf@iafe.uba.ar

1 Instituto de Astronomía y Física del Espacio (IAFE), CONICET-UBA, Buenos Aires, Argentina

2 Facultad de Ciencias Exactas y Naturales (FCEN), UBA, Buenos Aires, Argentina

3 LESIA, Observatoire de Paris, Université PSL, CNRS, Sorbonne Université, Univ. Paris Diderot, Sorbonne Paris Cité, 5 place Jules Janssen, Meudon, 92195 Paris, France

4 Instituto de Ciencias Astronómicas, de la Tierra y del Espacio (ICATE), CONICET, San Juan, Argentina

Published online: 19 December 2018

two processes, flux cancellation and bipole rotations, is at the origin of a series of events, homologous to the event we analyze in this article, which occurred in AR 11476 from 8 to 10 May 2012.

Keywords Active Regions, Models · Flares, Relation to Magnetic Field · Magnetic Reconnection, Observational Signatures · Surges · Jets

1. Introduction

Solar activity produces a variety of ejecta such as coronal mass ejections (CMEs), jets, surges, and sprays. They are usually classified according to their evolution, observed size, geometry, associated energies, and masses involved, but also according to the instruments, and hence wavelengths, with which they have been observed (*e.g.* Rust *et al.*, 1980).

Surges and sprays, in particular, have originally been identified in Hα images as the eruption of cold chromospheric material into the corona. While the material ejected in sprays apparently does not return to the coronal base, the material in surges decelerates and then falls down along the same magnetic structure through which it was originally ascending (Roy, 1973) and/or reaches the opposite end of the closed structure. Surges have typical velocities in the range of 50 to 200 km s^{-1}, they reach heights of up to 2×10^5 km, and have durations of a few tens of minutes (Foukal, 2004). They are often but not always observed in coincidence with the occurrence of flares (Schmieder *et al.*, 1988).

With the advent of extreme ultraviolet (EUV) instruments, it became clear that these ejections were also observable in this range (Schmahl, 1981). Multiwavelength analyses also demonstrated their connection with X-ray brightenings and jets (Harrison, Sime, and Pearce, 1990; Schmieder *et al.*, 1995; Canfield *et al.*, 1996). The main difference between surges and jets is their magnetic configuration, which is closed or open, respectively. Jet-like ejections observed in the EUV have been called EUV jets by some authors (Moore *et al.*, 2010; Liu and Kurokawa, 2004). Observed in this band, the typical temperature of the ejected material is of a few 10^5 K, while densities have been found to be in the range from 10^8 to 10^9 cm^{-3} (Raouafi *et al.*, 2016).

Concerning the photospheric magnetic field configuration where surges and jets occur, observations in the 1990s suggested that they could be indirectly caused by the emergence of parasitic polarities, accompanied sometimes by flux cancellation (see, *e.g.* Schmieder *et al.*, 1995; Canfield *et al.*, 1996; Chae *et al.*, 1999). High-resolution observations (Jibben and Canfield, 2004; Brooks, Kurokawa, and Berger, 2007; Guglielmino *et al.*, 2010; Uddin *et al.*, 2012; Vargas Domínguez, Kosovichev, and Yurchyshyn, 2014) also provide additional evidence for the close and repeated relation between flux emergence, chromospheric cold plasma ejections, and hot jets. Other investigations have shown that a combination of flux emergence and cancellation can play a role in the triggering of different types of jets (Liu *et al.*, 2011; Panesar, Sterling, and Moore, 2016), while in others, no flux emergence is observed (Young and Muglach, 2014a,b; Chandra *et al.*, 2017).

Based on several of the observations discussed in the previous paragraph and the pioneering flux-emergence model by Heyvaerts, Priest, and Rust (1977), Shibata *et al.* (1992) and Yokoyama and Shibata (1995, 1996) proposed a 2.5D numerical model in which the emergence of magnetic flux in an initial uniform coronal field could lead, via reconnection, to the ejection of cold plasma close to a hot jet. These authors described surges as resulting from a "sling-shot effect due to reconnection, which produces a whip-like [plasma] motion". Canfield *et al.* (1996), following the analysis of a series of Hα surges and related

X-ray jets, proposed a phenomenological 2D model based on reconnection to explain the observed evolution.

More recently, Moreno-Insertis and Galsgaard (2013) found a domain of dense cool plasma in their 3D magnetohydrodynamics (MHD) simulation of an emerging region. MacTaggart *et al.* (2015) performed 3D MHD simulations of the emergence of small-scale ARs in the presence of different ambient field configurations to determine where reconnection occurred and the characteristics of the flow of the dense plasma in different observed events. To understand the physical processes occurring in the photosphere, chromosphere, and corona during surges, Nóbrega-Siverio, Moreno-Insertis, and Martínez-Sykora (2016) performed a 2.5D radiative-MHD numerical simulation of the emergence of a twisted magnetic tube in a statistically stationary magnetoconvection configuration formed by the uppermost layers of the convective zone up to the corona. During the evolution of the system, part of the emerged cold and dense material is ejected as in a surge.

In the previously discussed models and simulations, magnetic reconnection is driven by flux emergence; however, in other simulations applied to jets, reconnection is forced by imposing horizontal photospheric twisting motions to a magnetic field configuration that includes a coronal magnetic null-point (Pariat, Antiochos, and DeVore, 2009, 2010; Pariat *et al.*, 2015, 2016).

Recent observations of coronal jets, either in coronal holes or in ARs, have identified the presence and eruption of small-scale filaments, called mini-filaments, which are part of the ejected material (Shen *et al.*, 2012; Adams *et al.*, 2014; Sterling *et al.*, 2015, 2016; Panesar *et al.*, 2016; Joshi *et al.*, 2018; Yang and Zhang, 2018; Moore, Sterling, and Panesar, 2018). In another example, where lower resolution observations were analyzed, the presence of a constantly reformed mini-filament and its eruption was postulated as the origin of a series of blow-out jets and the chain of consequent events (flares and narrow CMEs, Chandra *et al.*, 2017). In the observed examples, the mechanism associated with the destabilization of the mini-filament was the cancellation of magnetic flux along the polarity inversion line where it lay. Magnetic reconnection below the mini-filament was responsible for an observed flare, while the same mechanism above the mini-filament favored the injection of its material into open field lines to form the jet.

The identification of mini-filament eruptions as the main origin of the plasma ejected in jets led Wyper, Antiochos, and DeVore (2017) and Wyper, DeVore, and Antiochos (2018) to propose that these mass ejections are produced by a break-out mechanism similar to what has been proposed to explain larger events like CMEs (see, *e.g.* Karpen, Antiochos, and DeVore, 2012). In these simulations, an emerged bipole is embedded in a unipolar uniform ambient field where a 3D coronal null-point is present. A small flux rope or mini-filament is formed by shearing motions that also provide energy to the system. This strongly sheared field expands toward the null-point and a reconnection process occurs that, like in the standard breakout CME model, removes the field that restrains the small flux rope. Simultaneously, reconnection occurs below the small twisted flux rope as proposed in the articles mentioned in the previous paragraph, further building up the flux rope. Finally, reconnection between the twisted flux rope and the background open field launches a jet.

In several magnetic configurations associated with jets and surges, Hα brightenings at the event sites have a circular shape that can be closed (or almost closed, see, *e.g.* Joshi *et al.*, 2015; Sterling *et al.*, 2016; Li *et al.*, 2018). In magnetic field models where a null-point is found, the intersection of the separatrix (fan of the null) with the photospheric or chromospheric plane has a typical circle-like shape that agrees with observed chromospheric brightenings (see, *e.g.* Mandrini *et al.*, 2015; Masson *et al.*, 2012, 2017, for several examples). Null-point topology is also supported by a large number of jet observations (see the review by Raouafi *et al.*, 2016, and references therein).

Other magnetic topologies calculated from coronal extrapolation models have been found to be associated with jet and surge observations. Quasi-separatix layers (QSLs, see, *e.g.* Démoulin *et al.*, 1996, for the original definition) were identified by Mandrini *et al.* (1996) and Guo *et al.* (2013), without a magnetic null-point, in the case of jets. Hα surges were observed in magnetic configurations with QSLs by Cristiani *et al.* (2007) and in other configurations with bald patches by Mandrini *et al.* (2002). The latter topological structures were also observed during a series of blow-out jets and associated narrow CMEs by Chandra *et al.* (2017). Finally, the examples with and without a magnetic null-point are not conceptually different when considered from the QSL point of view, because a separatrix is only the extreme case when the field line mapping becomes discontinuous in the QSL core.

The event studied in this article is much less collimated than typical blow-out and EUV jets. Furthermore, like in surges, the material is ejected upward, stays enclosed in the magnetic structures of the active region, and falls back along these structures. We refer to this as an EUV "surge" event throughout because it is most prominent in this wavelength range. We use quotation marks to indicate that it is also different to the classical surges that have been analyzed elsewhere (see the references at the beginning of this section). This EUV event occurred in Active Region (AR) NOAA 11576 on 9 May 2012 and is associated with an M4.7 flare with a peak in GOES soft X-ray light curve at $\approx$ 12:32 UT. Preliminary results of our analysis were discussed elsewhere (López Fuentes *et al.*, 2015).

In Sections 2.2 – 2.8 we study the evolution of the event in several wavelengths using data from the instruments described in Section 2.1. After modeling the AR magnetic field and computing its coronal topology, in Section 3 we interpret the role of QSLs in the magnetic configuration, and we propose a phenomenological explanation of the event in terms of the eruption of the observed mini-filament and its interaction with the surrounding magnetic structure. In Section 4 we discuss our results and present concluding remarks.

2. Flare and EUV "Surge" Observations

2.1. Data Description

To analyze the events on 9 May 2012, we used EUV data from the *Atmospheric Imaging Assembly* (AIA: Lemen *et al.*, 2012) on board the *Solar Dynamics Observatory* (SDO), and from the *Sun-Earth Connection Coronal and Heliospheric Investigation* (SECCHI: Howard *et al.*, 2008) on board the *Solar Terrestrial Relations Observatory* (STEREO) spacecraft B, Hα data from the *H-alpha Solar Telescope for Argentina* (HASTA: Bagalá *et al.*, 1999; Fernandez Borda *et al.*, 2002), soft X-ray data from the *X-ray Telescope* (XRT: Golub *et al.*, 2007) on board *Hinode*, hard X-ray data from the *Reuven Ramaty High Energy Solar Spectroscopic Imager* (RHESSI: Lin *et al.*, 2002), and magnetograms from the *Helioseismic and Magnetic Imager* (HMI: Scherrer *et al.*, 2012) on board SDO.

EUV data from SDO/AIA correspond to the 304 Å and 171 Å channels (henceforth, AIA 304 and 171). We selected from full-disk images subimages containing AR 11576 for the temporal range corresponding to the analyzed event. By coaligning these images to compensate for solar rotation, we constructed the EUV movies that accompany this article (Section 2.4). The images used for the movies are represented in logarithmic intensity scale for better contrast. We complement the SDO/AIA data with observations from the 195 Å channel of the SECCHI instrument on board STEREO-B. We used the 195 Å band because it has the highest temporal resolution (5 minutes) of the SECCHI channels. On 9 May 2012,

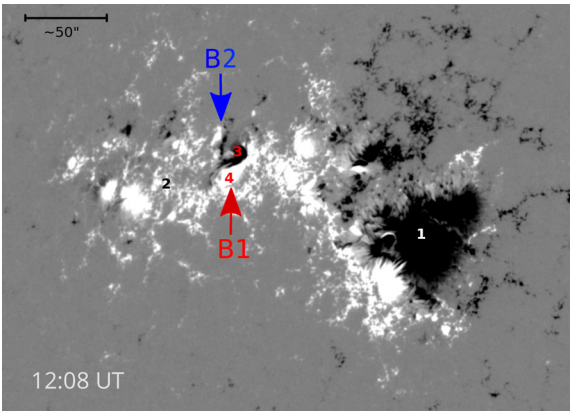

Figure 1 SDO/HMI LOS magnetogram of AR 11476, located at N12 E26, on 9 May 2012 at 12:08 UT. The *arrows* indicate the locations of the two rotating bipoles (*B1* and *B2*) described in Section 2.2. The flare and related "surge" originated in their vicinity. The polarities involved in the studied event are numbered: *1* and *2* for the AR polarities, and *3* and *4* for those of bipole *B1*. *Black* corresponds to negative magnetic field (pointing away from the observer), and *white* corresponds to positive field (toward the observer). The values of the field have been saturated above (below) 500 G (−500 G). The horizontal and vertical sizes of this image are 350″ and 250″, respectively. At the *top left*, a *black segment* has been added to the panel to indicate the approximate scale size. A movie showing the magnetic field evolution during three days (HMI.mp4) is attached as electronic supplementary material.

the STEREO-B spacecraft was located at an Earth ecliptic (HEE) longitude of −118° away from Earth. From this location, AR 11576 is seen at the solar limb.

The analyzed SDO/HMI data consist of line-of-sight (LOS) magnetograms of AR 11576, selected from full-disk data. These magnetograms were used to study the evolution of the AR magnetic field, as described in Section 2.2, and as boundary condition for the model described in Section 3.1.

The Hα data from HASTA have a resolution of approximately 2″ and are automatically taken in two different modes: normal (or patrol), and flare. In normal mode, during routine observations, the telescope takes full images once every 1 to 5 minutes. When a flare begins, the instrument changes to flare mode and images are taken up to a rate of 2 *per* s. The dataset used here consists of images taken in both modes depending on the time of observation: normal for before and after the analyzed flare, and flare mode during the event (see the description of the timing in Section 2.3). Similarly, *Hinode*/XRT images taken during the flare alternate between different filters (Ti-poly, Al-mesh, and Al-thick) and short or long exposure times. We combined these data in composite images in which the saturated pixels in the long-exposure images are replaced by the same corresponding pixels from the non-saturated short-exposure images. The XRT movie that accompanies this article has been made using these composite images (see Section 2.8). Finally, RHESSI-processed data correspond to hard X-ray counts in the channels of 10 – 30 keV and above 40 keV, integrated during periods of 20 s at the time of the soft X-ray GOES flare emission peak (at ≈ 12:32 UT, see Section 2.3).

2.2. Photospheric Magnetic Field Evolution

AR 11476 appeared on the eastern solar limb on 04 May 2012. By 06 May, it is clearly seen as having a global bipolar structure with a compact preceding negative polarity (numbered 1)

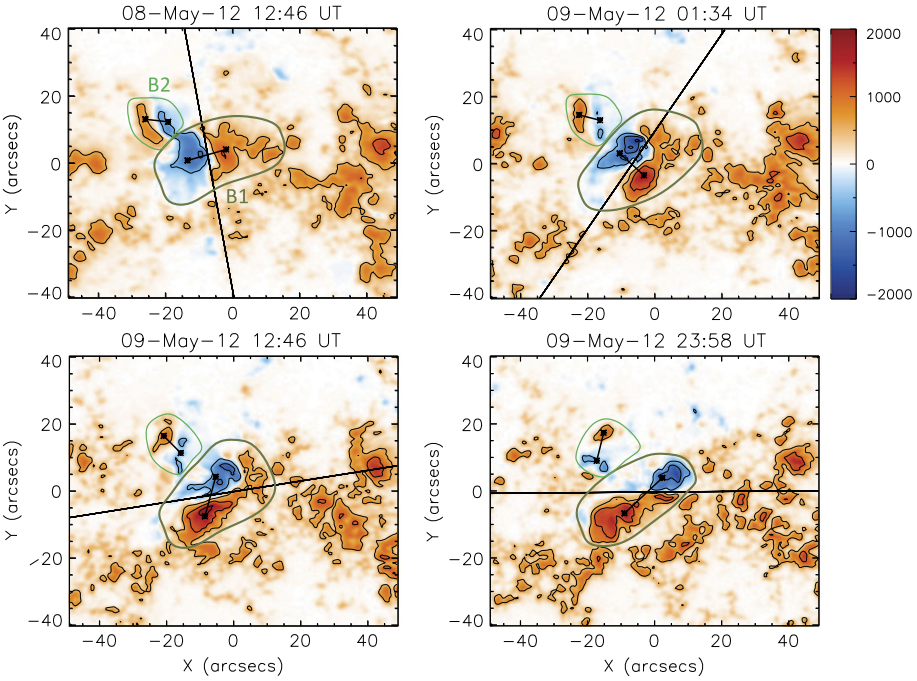

Figure 2 Four snapshots of the rotation of the bipoles B1 and B2. The dates and times are indicated at the *top* of each panel. The *short black segments* joining the *asterisks* (the positive and negative polarity barycenters) indicate the tilt angle. The *long black straight line* corresponds to the estimated mean polarity inversion line (PIL) of the largest bipole (B1). This bipole is enclosed by a *green contour* that surrounds the magnetic flux we used to compute its polarity centers and rotation, as also done for B2. In these magnetograms the *red* (*blue*) areas correspond to positive (negative) magnetic field. Magnetic field contours of ± 1000, 1500, and 2000 G are also included as reference. A movie included as electronic supplementary material shows the evolution of B1 (B1.mp4).

and a disperse following positive polarity (numbered 2) that presents substantial magnetic flux fragmentation. A small bipole was located at the center of the positive polarity, well visible on 07 May. However, as the AR evolved, what appeared to be a single bipole was identified to be, in fact, two independent bipoles (see the area within the black box in movie HMI.mp4 that is included as supplementary material). The two bipoles are identified as B1 and B2 (Figure 1). The negative and positive polarities of B1 are identified as 3 and 4, respectively. The flare and mass ejection occurred in their vicinity.

An analysis of the evolution of B1 and B2 starting 36 h before the studied events indicates a rapid clockwise rotation of both bipoles, which implies a fast injection of magnetic helicity whose characteristics depend on the magnetic connectivities. This helicity injection is associated with free magnetic energy accumulation and might also contribute to the mini-filament destabilization, as proposed by Wyper, Antiochos, and DeVore (2017) and Wyper, DeVore, and Antiochos (2018). The panels of Figure 2 show four different stages of the rotation of the bipoles. The full evolution can be seen in the movie that accompanies this article (B1.mp4).

The rotation of each bipole also implies the rotation of their polarity inversion lines (PILs). The long black straight line in Figure 2 and in the corresponding movie is the PIL of B1, which we computed following the procedure developed by Poisson *et al.* (2015). The

position of this straight line is defined to best separate the negative and positive polarities of bipole B1. Following Poisson *et al.* (2015, 2016), the shape of the polarities at both sides of the PIL is an indication that the bipole was formed by a negative twisted flux rope.

To characterize the rotation quantitatively, we followed the evolution of the tilt angle of the two bipoles. We first computed the barycenter positions of their positive and negative polarities (indicated by asterisks in Figure 2) while limiting the computation to the bipoles themselves, *i.e.* to the flux encircled by the green curve for B1 and B2, as shown in Figure 2. Then, we defined the tilt angle as the angle that the segment that joins the two barycenters forms with the solar equator direction. The evolution of the segment indicates that B1 rotated by approximately 140° clockwise for 36 h before the flare and continued to rotate $\approx 40°$ more until 10 May around 22:00 UT. In the case of B2, the rotation before the ejection and flare on 9 May was $\approx 50°$ clockwise and continued for another 50° in the same sense, until it disappeared entirely by $\approx$ 10:00 UT on 10 May.

In the time period that we measured the rotation of the two bipoles, their magnetic flux decreased steeply as it cancelled with the surrounding magnetic field and probably also dispersed in the case of B2. The negative flux of B2 clearly decreases against the positive flux concentration to the west (see HMI.mp4). As discussed in Section 3.4, this flux cancellation together with the rotation of B1 might play a key role in triggering the mini-filament eruption. The magnetic flux of B1 decreased by about 90% from 8 May until 10 May at $\approx$ 22:00 UT.

2.3. Chromospheric Evolution

An M4.7 flare was observed to start at 12:23 UT in GOES soft X-ray light curve (SOL20120509T12:23:0) with a maximum at $\approx$ 12:32 UT. Figure 3 shows Hα images from HASTA at six different times during the flare evolution. A movie starting at 11:55 UT and ending at 13:15 UT is included as electronic supplementary material (HASTA.mp4). The cadence in the data changes in the movie as the telescope changes to flare mode at about the start time of the flare ($\approx$ 12:23 UT). The data acquisition returns to the normal cadence (an image every 2 to 4 minutes) at about 12:37 UT.

Figure 3a shows the AR at approximately the time at which the flare started. Magnetic field contours are overlaid as a guide to the photospheric counterpart of the observed Hα brightenings. To improve the visibility of the surge in the HASTA data, we applied a cross-correlation technique to minimize the atmospheric jitter of the images. In order to increase the contrast of the moving material and any brightness variation in the data, we constructed a base difference image sequence by subtracting from each image of the set the pre-event image obtained at 12:23:51 UT. We refer to the images processed in this way as base difference images throughout. Panels b, e, and f of Figure 3 are base difference images. We also include as supplementary material a movie containing the obtained sequence of base difference images (HASTA-diff.mp4).

In Figure 3b we show a base difference image at $\approx$ 12:27 UT. In this panel, we identify an elongated brightening to the west that coincides in location with part of the negative B1 polarity and corresponds to flare kernels. A weaker brightening is seen to the northeast (see the thick white arrow). This brightening elongates to the north, and when we compare this image and its corresponding movie with the AIA 304 observations of Figure 5b and its corresponding movie, we conclude that it corresponds to heated surge material seen as it starts moving upward. As the flare developed (Figure 3c), another elongated kernel became visible to the east of the first, labeled k2, and a distant and extended kernel became prominent on the opposite side of the AR, labeled k1. These kernels are also present in AIA 304 images

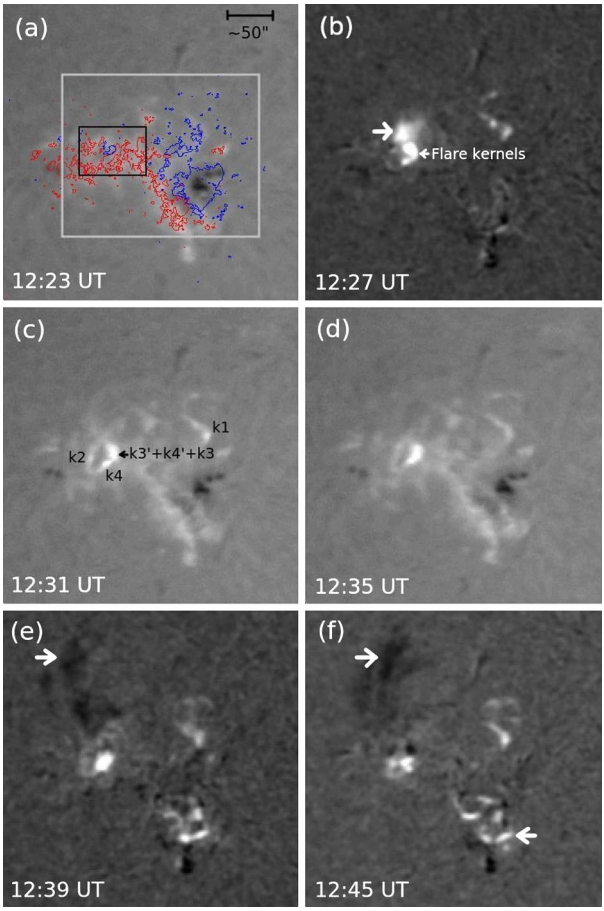

Figure 3 HASTA images showing the flare evolution. The times are indicated in the *bottom left corners* of each panel. In panel **a**, ± 300 G HMI *contours* are included as reference. As in Figure 2, *red* (*blue*) corresponds to positive (negative) magnetic field. A *black box* is added to indicate the location of bipoles B1 and B2. It approximately covers the FOV of the panels in Figure 2. The *larger gray box* indicates the FOV of Figure 4. A *black segment* has been added in the *top right corner* to indicate the scale size. Panels **b**, **e**, and **f** correspond to base difference images (see Section 2.3). The *white arrow on the left* in panel **b** points to a northeastern brightening that probably corresponds to heated surge plasma as it starts to flow upward (see also the movie surge-closeup.mp4 that accompanies this article). In panel **c**, the flare kernels are labeled *k1* – *k4* following the numbering used to label the magnetic polarities in Figure 1. *k3′* and *k4′* indicate the kernels associated with the footpoints of loops that result from the internal reconnection process described in Section 3.4. The brightening indicated with a *black arrow* and identified with the label $k3' + k4' + k3$ is composed of these three kernels (see also Figure 4d). The *upper white arrows* in panels **e** and **f** shows the location of the surge. The *lower white arrow* in panel **f** points to a second flare that is unrelated to the event studied in this article (see text in Section 2.3). A movie showing the Hα evolution (HASTA.mp4) is attached as electronic supplementary material. The square panels have a side length of approximately 380″.

taken at the same times (Figure 5). From comparing Figures 3 and 5 and according to the analysis of Section 3.4, we conclude that the brightening labeled "Flare kernels" in Figure 3b corresponds to the overlapped emission of kernels k3′, k4′, and k3, while k4 is the smaller kernel at the southeast (see labels in Figure 3c). A second series of brightenings (indicated

with a white arrow in panel f) are observed in the southwest portion of the AR at later times (Figure 3e – f), which are apparently not related to the flare we studied.

Although barely discernible, we identify in Figure 3e – f the surge (indicated with white arrows) as a dark feature in absorption northeast of the AR. The surge can also be appreciated in absorption in the Hα movies that accompany this article (HASTA.mp4 and HASTA-diff.mp4), where it is seen in motion.

For a better identification of the Hα features and their comparison with AIA observations, we show in Figure 4a a zoomed-in image of the area indicated with a gray box in Figure 3a at a time just before the event (12:20 UT). Note the circle-shape brightening, indicated with a white arrow to the left, that surrounds the negative polarity of B1, part of its positive polarity, and all of B2, as described in Section 2.2. This circular brightening is also observable in AIA 304 (also indicated with a white arrow in Figure 4c) since around 08 May. The presence of this circular brightening strongly suggests that energy release at a very low rate was occurring, accompanying the rotation of the bipoles probably because of their interaction with the overlying magnetic field. The identification of these kernels is confirmed by a close inspection of the AIA 304 image shown in Figure 4d, where they are labeled individually. The kernels k3′ and k4′ are associated with the footpoints of loops that result from the internal reconnection process that we thoroughly described in Section 3.3. Later on, the kernels extend, and after the flare peak (12:32 UT), their intensity decreases.

2.4. EUV Evolution from the Earth Point of View

In AIA 304 images we also observe bright areas at the location of the Hα plage regions, as expected. For a better comparison, in Figure 4c we show the same area (indicated with a gray box in Figure 3a) for AIA 304 before the event (12:20 UT). The white arrows indicate the circle-shaped brightening that surrounds the negative and part of the positive polarities of B1 and all of B2 (on the left) and the elongated distant kernel k1 (on the right).

As described in Section 1, recent observations relate jets to the eruption of mini-filaments, which, as the word indicates, are smaller versions of normal large-scale filaments. High-resolution observations such as those currently obtained with imagers like SDO/AIA allow us to identify structures that were unobservable with the previous generation of solar instruments. Figure 4c shows an elongated dark structure along B1 PIL compatible with the presence of a mini-filament (see the black arrow in this panel). We also include a movie of this region as supplementary material (surge-closeup.mp4) with a high temporal resolution (5 images *per* minute) showing the destabilization and eruption of the mini-filament. In Section 3.4 we analyze and discuss the role of this structure in the events we studied.

Figures 5 and 6 show AIA 304 and 171 images at approximately the same times as those of HASTA in Figure 3. An HMI magnetogram contour is overlaid on the image in Figure 5a as a reference. In panels b – e of Figure 5, as for the Hα images, the main flare kernels are seen at the site of the main rotating bipole. The most striking feature in Figures 5 and 6 is the dense EUV surge that moves toward the northwest part of the main negative AR polarity (numbered 1). This evolution starts right after the first appearance of the flare kernels. This is better seen in the corresponding movies that accompany the article as supplementary material (AIA171.mp4, AIA304.mp4, and surge-closeup.mp4). The ejected material is seen to ascend fast along the magnetic structure overlying the main bipole. This is clearer in the AIA 171 images in Figure 6, where the AR loop structure before and during the event is well observed.

We can roughly estimate the mean velocity of the EUV surge front in the plane of the sky. Since the surge motion is dominantly northward, we chose to follow the northward motion

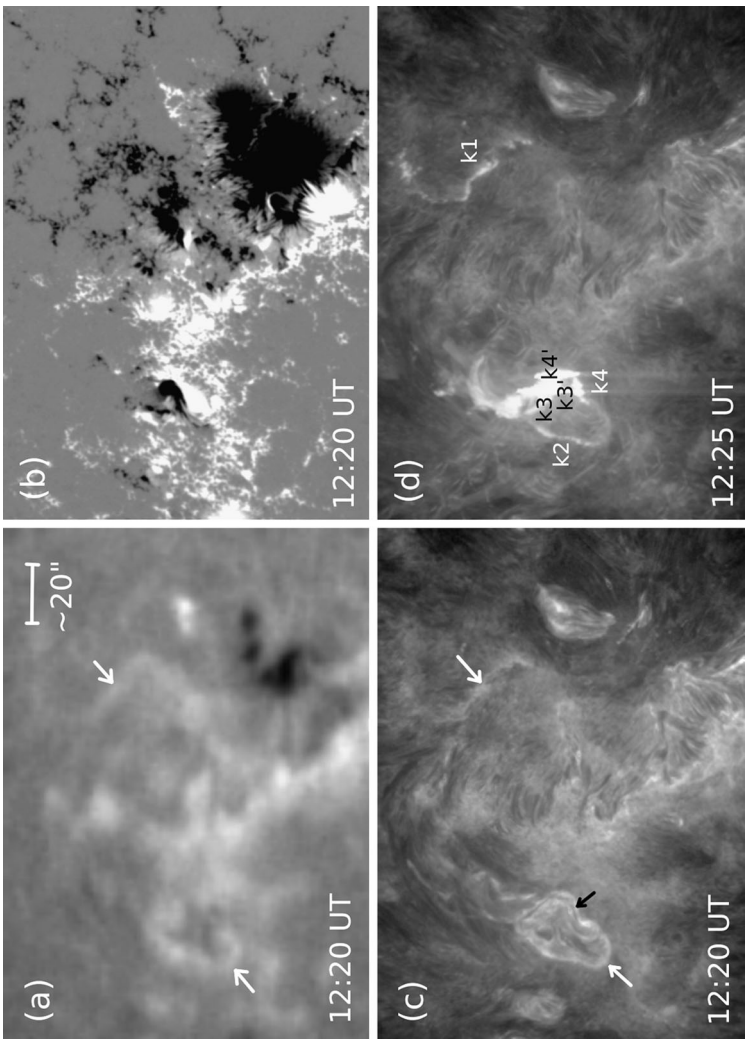

Figure 4 (**a**) Enlarged view of the field covered by the *gray box* in Figure 3a at a time previous to the event. The *white arrow on the left* indicates the circular brightening that partially surrounds bipoles B1 and B2 (see Section 2.2). The *white arrow on the right* indicates a brightening on the main negative polarity of the AR. The *white segment* at the *top right* of the panel is added to indicate the approximate scale size of the images. (**b**) Same FOV for HMI data for reference. (**c**) Same FOV for AIA 304 data (see also Figure 5). The *white arrows* indicate the same corresponding features as in panel **a**, and the *black arrow* indicates the location of the mini-filament. (**d**) AIA 304 image close to the event start time. Kernels *k1* to *k4*, *k3′*, and *k4′* are indicated. See also the accompanying movie that is included as supplementary material (surge-closeup.mp4).

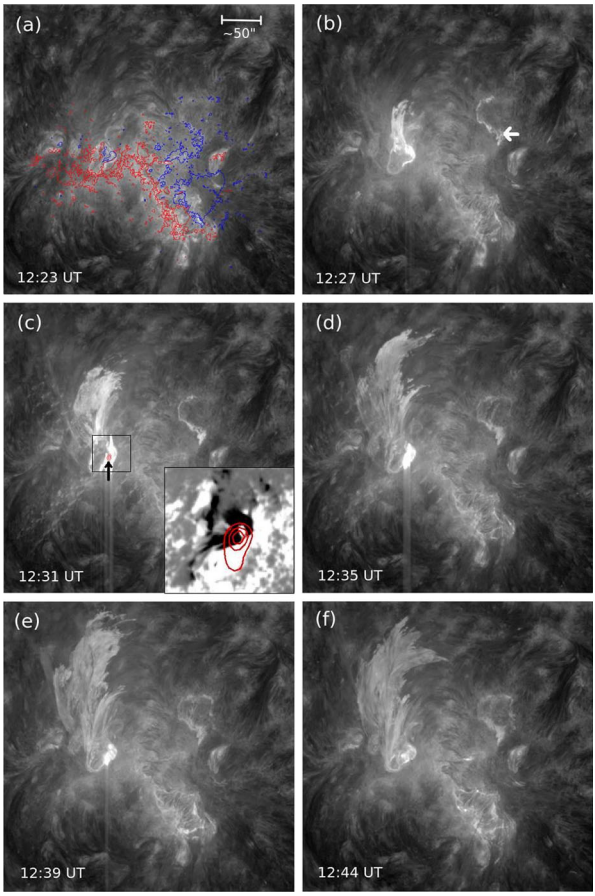

Figure 5 SDO/AIA 304 images for the same times as those in Figure 3. Times are indicated in the *bottom left* of the panels. Panel **a** includes ± 300 G HMI contours as reference. *Red* (*blue*) corresponds to positive (negative) magnetic field. A *white segment* has been added on the *top right* of the panel **a** to indicate the approximate scale size. Panel **c** shows the location of RHESSI 40 – 80 keV contours (in *red*) at 40, 60, and 80% of the maximum, integrated between 12:31:56 and 12:32:16 UT (around the time of the peak emission of the flare in soft X-rays). A *small black arrow* is added to facilitate viewing the location of the RHESSI contours. The *inset* in the *lower right corner* of this panel is a zoom of the *rectangle* that surrounds the brightest region in this AIA image. RHESSI contours in the *inset* are overlaid on the corresponding HMI magnetogram. A movie showing the AIA 304 evolution (AIA304.mp4) is attached as electronic supplementary material. The square panels have a side length of approximately 380″. The *inset* in panel **c** covers approximately 50″ × 50″.

of the leading point of the front as a proxy for the surge velocity projected onto the plane of the sky. We obtain a value of ≈ 90 km s^{-1}, which agrees with the typical values measured in other surge events (see references in Section 1).

As observed in the AIA 304 and 171 movies, as soon as the EUV surge reaches its maximum height, part of the material drains toward the western footpoints of the loops along which it moves, and part drains back to their eastern footpoints. The western loop footpoints, containing the draining plasma, end at the flare kernel k1, as observed both in Hα and AIA 304 images (Figure 3c and Figure 5b). The intensity of this region increases simultaneously with the flare.

As previously reported (*e.g.* Canfield *et al.*, 1996; Chae *et al.*, 1999) and also observed in the EUV movies that accompany this article (AIA171.mp4, AIA304.mp4), the upward motion of the surge material has a torsional component. We associate the helicity accumulation with the precursory rotation of the bipolar structures described in Section 2.2 and its release in large-scale AR loops as due to the magnetic reconnection process associated with the flare. Although a rotational component is evident in the evolution of the surge observed in AIA 171 and 304 data, the complex structure of the ejected material as projected onto the plane of the sky makes it very difficult to obtain a definite answer regarding a sense of rotation, and a quantitative estimation of this rotation is even more difficult.

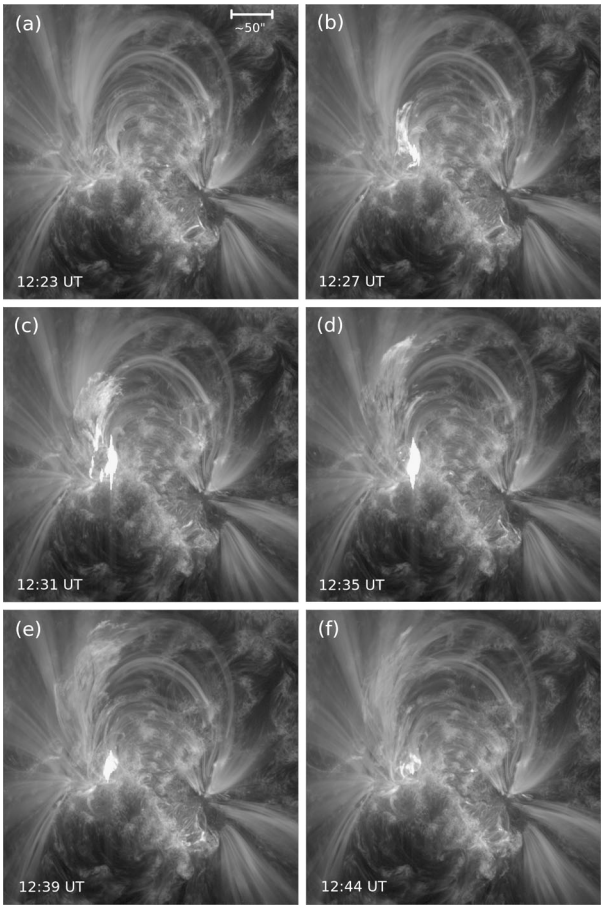

Figure 6 SDO/AIA 171 images for the same times and FOVs as in Figures 3 and 5. The corresponding times are indicated in the *bottom left* of the panels. A *white segment* has been added on the *top right* of the panel **a** to indicate the approximate scale size. These images show the evolution of the EUV "surge" and also part of the global structure of the AR as revealed by long EUV loops. A movie showing the AIA 171 evolution (AIA171.mp4) is attached as electronic supplementary material.

When we compare the evolution of the surge in Hα and AIA 304 (Figures 3 and 5), the surge seems to start with the ascent of material at the 304 Å temperature range. We first see a bright elongation in HASTA images toward the north at ≈ 12:27 UT; the surge is more prominent in AIA 304 at the same time, while it is only later that the material is observed to barely expand in absorption in Hα when we compared the images in AIA 304 at the same times (Figure 3e – f to Figure 5e – f). Assuming that reconnection between the erupting mini-filament and the overlying field starts at low coronal heights, we expect to see the evolution we just described. First, the plasma is heated up, rises, and is seen bright in Hα and dominantly in 304 Å. Then, part of the ejected material cools down and becomes visible in absorption in Hα.

The circle-shaped brightening around the bipoles and their sustained rotation, from before the event analyzed in this article and until more than a day after (10 May at around 22:00 UT for B1), motivated us to search for similar patterns of activity in this range of time. Using Helioviewer (https://helioviewer.org/), we are able to identify four additional EUV surges in AIA 304, associated with M-class flares, one on 8 May at ≈ 13:05 UT (flare M1.4), another on 9 May at ≈ 21:05 UT (flare M4.1), and two on 10 May at ≈ 04:15 UT (flare M5.7, see, *e.g.* Yang and Zhang, 2018) and at ≈ 20:25 UT (flare M1.7). All these flares and surges started where the two rotating bipoles were located and the plasma evolved

along large-scale loops with footpoints on the negative main AR polarity (numbered 1) to the west, as is the case of the event studied in this article. This implies a recurrence of energy storage, probably mini-filament rebuilding, as proposed by Chandra *et al.* (2017) (see also the simulations of Wyper, Antiochos, and DeVore, 2017; Wyper, DeVore, and Antiochos, 2018), and energy release processes with a timescale of between 7 and 23 hours and a mean of about 14 hours.

2.5. EUV Evolution from the STEREO-B Point of View

Complementing AIA data, we used SECCHI observations from STEREO-B, which at the time of the event was located toward the east solar limb as observed from Earth. From the STEREO-B point of view, AR 11476 appeared on its northern right solar limb, as shown in Figure 7. The panels of this figure correspond to different times in the SECCHI 195 Å channel closest to the times of Figures 5 and 6. We used this wavelength because it has the highest available temporal resolution (5 minutes). We also produced a SECCHI 195 Å movie that covers the evolution from 12:00 UT to 14:55 UT (see STEREOB-195.mp4 included as supplementary material). This movie and Figure 7 illustrate the evolution of the flare and EUV surge as observed at the limb by STEREO-B, above a series of pixels that are saturated because of the flare.

The vantage point of view of STEREO-B provides information on the EUV surge structure that is inaccessible from Earth's line of sight. For instance, an estimation of the surge velocity using STEREO-B data gives $\approx 120\ \mathrm{km\,s^{-1}}$ in the plane of sky, which is consistent with typical velocity values cited in Section 1. For this computation, we followed the central point of the leading edge of the surge seen against the dark and less dense background. The northward component of this motion is $\approx 98\ \mathrm{km\,s^{-1}}$. Considering that both spacecraft are located at Earth's ecliptic plane, this value is consistent with the $90\ \mathrm{km\,s^{-1}}$ computed for the northward motion of the surge as observed in the plane of the sky by the SDO. The small difference is likely due to the geometrical (different plasma depth columns) and temporal (different instrumental cadences) differences, the errors involved, and the fact that observations correspond to different wavelength bands (304 Å and 195 Å) with different temperature responses.

2.6. Estimation of Temperature and Density

The observed width of the EUV surge from a direction that is almost perpendicular ($\approx 118°$) to the SDO line of sight lets us also estimate the depth of the emitting material observed by AIA. We can use this information to roughly calculate the temperature and density of the surge plasma by applying the so-called filter ratio technique to the AIA 171 and 304 observed intensities. The procedure consists of assuming a quasi-uniform temperature for the surge plasma. In this case, the intensity observed in a given AIA channel can be considered to be the emission measure [EM] of the plasma multiplied by the instrument response function in that channel, $I_{\mathrm{ch1}} = \mathrm{EM}\ S_{\mathrm{ch1}}(T)$ (see, *e.g.* López Fuentes, Klimchuk, and Mandrini, 2007). In this way, the ratio of the intensities in two different channels is a function only of the temperature, $R(T) = I_{\mathrm{ch1}}/I_{\mathrm{ch2}}$. By inverting this function, we obtain T. When the temperature is known, the density is computed from $n_{\mathrm{e}} = [\mathrm{EM}/(f d)]^{1/2}$, where f is the filling factor and d is the depth of the observed plasma column.

We applied this procedure to the intensities averaged on the same corresponding surge areas observed in AIA 171 and 304. We computed this at the time when the EUV surge had its maximum apparent volume (at $\approx$ 12:39 UT). We determined a temperature of 2×10^5 K.

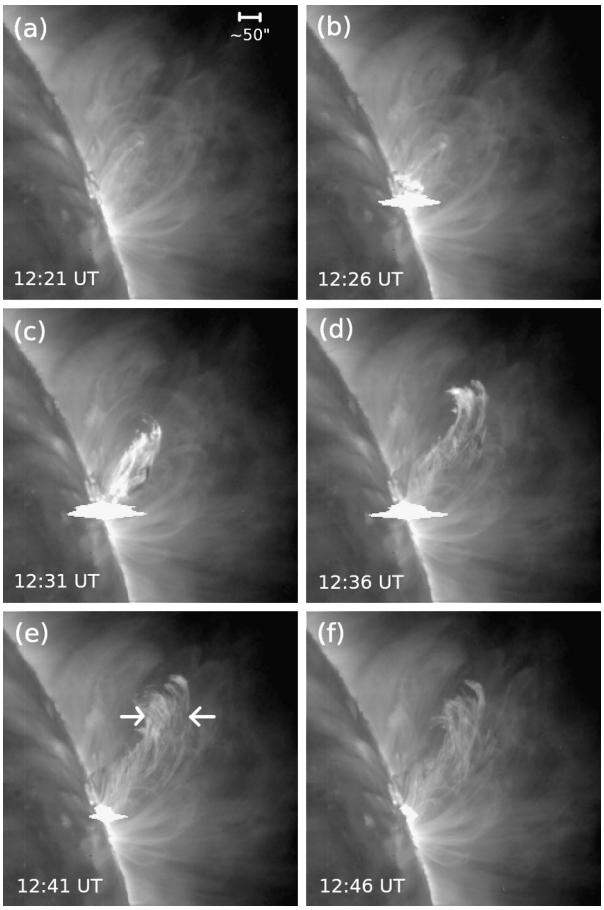

Figure 7 STEREO-B/SECCHI images of AR 11476 in the 195 Å channel. At the date of observation, the spacecraft was approximately located on the ecliptic at 118° east of Earth. From this position, the AR is observed on the solar limb. The saturated pixels correspond to the flare. The EUV surge evolution is clearly identifiable in the images. The observation times are provided in the *bottom left corner* of the panels and are as close as possible to those of Figures 3 – 6. A *white segment* has been added in the *top right corner* of panel **a** to indicate the figure scale–size. A movie (STEREOB-195.mp4) showing the evolution of the EUV surge in SECCHI images is attached as electronic supplementary material.

Using the width of the EUV surge observed by SECCHI, which is estimated to be approximately 50 Mm (indicated with white arrows in Figure 7e), as the depth of the plasma column [d] observed by AIA and setting $f = 1$, we obtain $n_e = 1.8 \times 10^9$ cm^{-3}.

We repeated the computation by subtracting a mean of the background on both sides of the surge for both AIA bands. For AIA 304, the background is very small compared with the surge intensity, but for AIA 171, the background can be as high as 80% of the surge intensity. Moreover, due to the presence of AR coronal loops, the AIA 171 background tends to be particularly noisy in the vicinity of the surge. Therefore, different background choices provide a variety of temperature results. By trying different background combinations, we obtain temperature values between 1.4 and 1.8×10^5 K and corresponding densities from 1 to 1.5×10^9 cm^{-3}. These values continue to be within the ranges measured in previously studied surge events (see references in Section 1). A larger effect on the derived density comes from the assumed filling factor, since if $f \approx 0.1$, it implies a factor of ≈ 3 on the computed density. Then, the obtained densities are lower limits if $f < 1$.

Interestingly, although it is progressively less visible for hotter AIA bands, the surge is still observable in AIA 193 and 211. Applying the filter ratio technique, using the same surge and background selection as above, we obtain for the 193/171 combination $T = 1.5 \times 10^6$ K and for the 193/211 combination $T = 1.8 \times 10^6$. In both cases, $n_e \approx 1 \times 10^8$ cm^{-3}, more

than one order of magnitude smaller than for the 304/171 combination. This confirms that the bulk of the mass of the surge emits at a temperature around the maximum AIA 304 response, while surprisingly, the plasma pressure is comparable when using all ratio pairs.

2.7. Hard X-Ray Evolution

RHESSI data in the 10 – 30 keV and 40 – 80 keV bands integrated during 20 s at the time of the flare peak (≈ 12:32 UT) indicate hard X-ray emission in a very concentrated area close to the first Hα elongated kernel (see Figure 5c). A small black arrow is added to indicate the location of RHESSI contours in the AIA 304 image. The observed RHESSI emission is also close to the location of the mini-filament (see Section 2.4) whose eruption was at the origin of the events described in this article. The inset in Figure 5c shows (in red) an overlay of the RHESSI 40 – 80 keV contours at 40, 60, and 80% of the maximum on a simultaneous HMI magnetogram. Note that the estimated error in the location of the RHESSI high-energy source, coming from the processing procedure and coalignment between different instruments, is around 5″ (Lin *et al.*, 2002).

The magnetogram in the inset shows a region of pixels displaying a magnetic field sign reversal with apparent positive (in white) polarity within the negative polarity of the main rotating bipole (compare with the magnetogram of Figure 1, taken at 12:08 UT). This type of anomaly has been observed in *Michelson Doppler Imager* magnetograms at locations where beams of high-energy particles precipitated at the maximum of some flares; see an explanation and the example shown by Qiu and Gary (2003) and another example in Mandrini *et al.* (2006). Taking into account the uncertainty in the location of RHESSI sources, the field sign reversal region would agree with the highest intensity RHESSI contour.

2.8. Soft X-Ray Evolution

Figure 8 shows the evolution of the flare observed with *Hinode*/XRT. Panels a – d of Figure 8 are for the same times as the corresponding ones in Figures 3 – 6. Figure 8e and f show images at slightly later times (4 and 12 minutes later than the corresponding panels of Figures 3 – 6). An XRT movie showing the evolution from 12:17 UT to 13:52 UT is available as electronic supplementary material (XRT.mp4). The flare onset appears in the XRT images as an intensity increase in small elongated loop-like features at the location of the bipoles. Note in Figure 8c – d the vertical set of dark pixels that corresponds to the saturated area of the images, which has been replaced with the corresponding pixels from images with shorter exposure times. Some of the pixels in these areas look black because the composite routine sets a value 0 to the pixels from the short exposure images that have intensities below the minimum of the long-exposure images. Despite this, the bright loop-like features associated with the flare are clearly discernible in these images.

A set of longer loops connects the AR zone around the small bipoles to the western portion of the AR. These loops increase both in intensity and projected height as the extension and brightness of the flaring area increases (Figure 8c – d). The time at which this set of long loops reaches its maximum projected height coincides with the time at which the surge observed in the EUV bands reaches its maximum height and apparent volume (around 12:39 UT).

A few minutes after the soft X-ray intensity peak, during the gradual phase of the flare (Figure 8e – f), two clear sets of loops are identifiable: short (low-lying) very bright loops at the location of the rotating bipoles, and long loops that connect to the western part of the AR. The footpoints of these two sets of loops agree with the flare kernel locations in the Hα

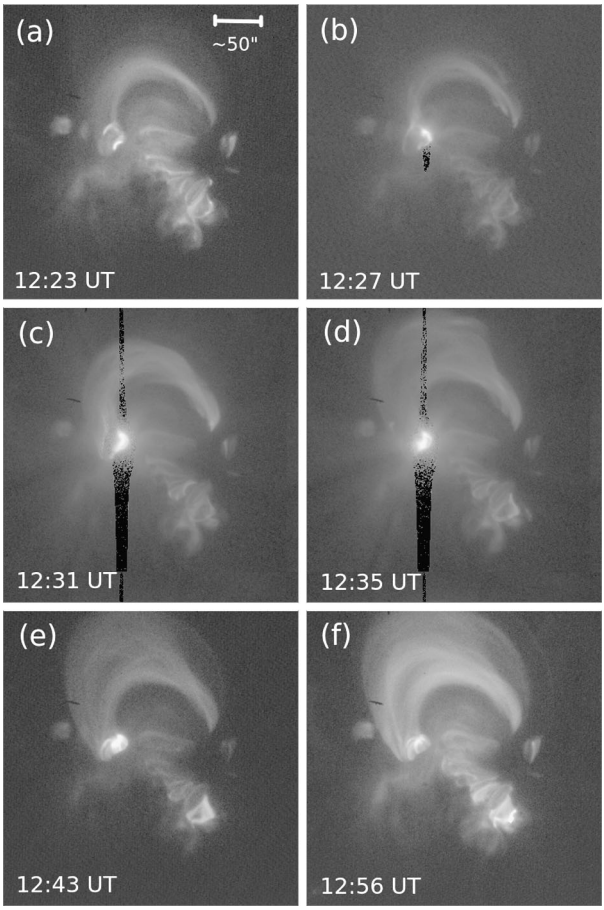

Figure 8 *Hinode*/XRT images of AR 11476 for different times along the analyzed event evolution, but as close as possible to those of Figures 3 – 6 and with the same FOV. The times are shown in the *bottom left corners* of the panels. A *white segment* has been added in the *top right corner* of panel **a** to indicate the figure scale–size. Images in panels **b**, **c**, and **d** are composites of images with short and long exposure times. The series of *black pixels* seen in these images are due to the effect of the composition. The bright structures associated with the flare are clearly seen in panels **a** to **d**. Their locations agree with those of the magnetic bipoles described in Section 2 and shown in Figure 2. A movie (XRT.mp4) showing the evolution of the large-scale loops in XRT images is attached as electronic supplementary material.

images (Figure 3) and in AIA 304 images (Figure 5). The topological analysis of the AR structure (Section 3) will help us understand the role of these observed structures.

Finally, it is also worth mentioning that when we compare the timing of the AIA 304 and XRT movies (AIA304.mp4, XRT.mp4), the XRT set of large-scale loops has a much longer duration than the surge. The loops remain bright well after the surge material has fallen back to the chromosphere.

3. Magnetic Field Topology of the Flare and EUV Surge Region

3.1. The Coronal Field Model

To understand the role of the magnetic structures in AR 11476 during the flare and EUV surge, we first modeled its coronal field and later computed its magnetic topology. We extrapolated the HMI LOS magnetic field to the corona using the discrete fast Fourier transform method described by Alissandrakis (1981) under the linear force-free field (LFFF) approach ($\nabla \times \boldsymbol{B} = \alpha \boldsymbol{B}$, with α constant).

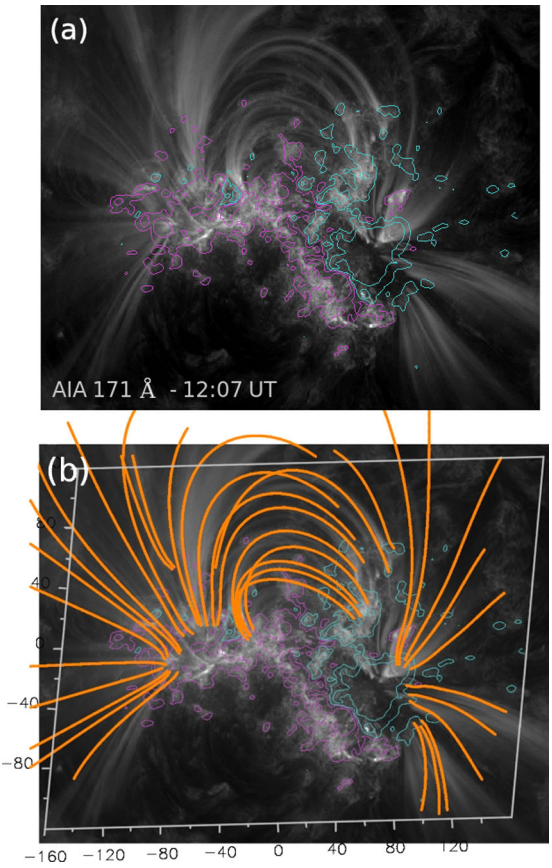

Figure 9 (**a**) SDO/AIA 171 image at 12:07 UT overlaid with HMI isocontours with the same values as those in panel **b**, *magenta* (*blue*) for positive (negative) values of the field. (**b**) Coronal magnetic field model of AR 11476 overlaid on the 171 Å image in panel **a**. Magnetic field lines (*thick continuous orange lines*) have been superimposed to be compared to the AR loops (see Section 3.1 for the details on the model and α values). Isocontours of the field of $\pm$ 100 and 500 G for positive (negative) values are shown in *magenta* (*blue*). The axis coordinates are in Mm in panel **b**; these are the units we used to compute the model. The inclination of these axes indicates that the AR is slightly away from the disk center as seen from the perspective point of view of an observer at Earth.

Figure 9a shows an AIA 171 image before the flare (12:07 UT) in which large-scale magnetic loops are visible. Figure 9b displays the coronal model overlaid on the same AIA image. We used the HMI magnetogram that was closest in time as the boundary condition for the model. We also applied a transformation of coordinates from the local frame (in which the computations are made) to the observed one so that our model can be compared to the flare brightenings and the EUV surge loops. Although this model cannot take into account the distribution of currents at the photospheric level and the strong shear that the rotation of the bipoles could have created but only the shear in the global magnetic configuration, it is fast and has proven to be efficient in computing the magnetic field topology that is to be compared with observed active events (see references in Section 3.2). Therefore, our magnetic field model and the following topology computation represents the global AR magnetic structure (see Section 3.2).

The value of α, the free parameter of the model, was set to best match the observed loops (as discussed by Green *et al.*, 2002). The best-matching value for the larger scale loops is $\alpha = -6.2 \times 10^{-4}$ Mm^{-1}, while for the shorter loops in the same image, it is -3.1×10^{-3} Mm^{-1}. This large-scale non-potentiality is related to the main AR polarities and not to the small rotating bipoles. The AR appears on the eastern solar limb already emerged, therefore we cannot determine its age. However, its photospheric magnetic field, with strong sunspots that still have a distribution showing magnetic tongues (Figure 1), indicates that it is a young AR close to its maximum flux stage. The tongue-like pattern (see

Poisson *et al.*, 2015) present for the main polarities of the AR is compatible with the sign of α.

3.2. Quasi-Separatrix Layers

Démoulin *et al.* (1996) introduced the concept of quasi-separatrix layers (QSLs). They are 3D thin volumes where the coronal field-line connectivity experiences a drastic change. QSLs are preferred sites for the formation of current layers and are therefore locations where magnetic reconnection is expected to occur. Several numerical experiments support this idea (see, *e.g.* Milano *et al.*, 1999; Aulanier, Pariat, and Démoulin, 2005; Büchner, 2006; Pariat, Aulanier, and Démoulin, 2006; Wilmot-Smith, Hornig, and Pontin, 2009; Effenberger *et al.*, 2011; Savcheva, van Ballegooijen, and DeLuca, 2012; Janvier *et al.*, 2013).

As concerns solar active phenomena, the computation of QSLs helps to interpret where flare kernels or other energy release manifestations should be observed (*e.g.* Démoulin *et al.*, 1997; Bagalá *et al.*, 2000; Mandrini *et al.*, 2006, 2014, 2015; Cristiani *et al.*, 2007; Zhao *et al.*, 2014; Savcheva *et al.*, 2015; Janvier *et al.*, 2016; Polito *et al.*, 2017; Joshi *et al.*, 2017). Furthermore, for moderately sheared or twisted magnetic structuring, the properties of QSLs in complex (multi-polar) configurations depend strongly on the photospheric distribution of the vertical field component and weakly on the details of the magnetic field model (*i.e.* the spatial distribution of α). In this sense, QSLs are a strong tool for understanding where energy release proceeds during active phenomena and for learning about the properties of energy release sites (see the reviews by Longcope, 2005; Démoulin, 2006; Mandrini, 2010).

The original method for determining the location of QSLs was described by Démoulin *et al.* (1996). QSLs were defined using the norm of the Jacobian matrix of the field-line mapping. In this method the value of the norm depends on the direction chosen to compute the mapping (from positive to negative photospheric polarities or the reverse). Then, the norm has different values at the two footpoints of a field line in the photosphere. This ambiguity was solved by Titov, Hornig, and Démoulin (2002), who defined the squashing degree [Q], which is independent of the mapping direction. Q is the norm squared divided by the ratio of the vertical component of the photospheric field at both ends of a field line. In this way, Q could be assigned to have a constant value along each field line. QSLs are computed by integrating extremely high numbers of field lines in a very precise way. To decrease the computation time, we used an adaptive mesh to progressively refine the computation of field lines where Q has the highest values. We followed this iterative method until the QSL was locally well resolved or when the limit of the integration precision was reached (see more details in Mandrini *et al.*, 2015).

As in other previous examples, we selected high values of Q to show the extension of the QSL traces at the photospheric level. Figure 10 displays the location of the intersection of QSLs with the photospheric plane. These photospheric traces were computed using the same HMI magnetogram as shown in Figure 9, when the magnetic data do not show unrealistic values because of the injection of high-energy particles in the photosphere (see the inset of Figure 5c). The results shown were computed with the highest $|\alpha|$ value, but similar results were obtained with the lowest $|\alpha|$ value (Section 3.1). QSL traces, shown as black continuous thick lines for simplicity and clarity, are overlaid on the photospheric magnetogram indicated as isocontours of the vertical component of the magnetic field. The value of Q for all QSL traces stays above 10^8, implying that these QSLs are very thin.

Panel a of Figure 10 depicts an image of AIA 304 where the circular brightening at the location of the bipoles, the surge at an early stage, and the far AIA 304 kernel, k1, on the main AR negative polarity, are observed. By comparing this with panel b, which is at the

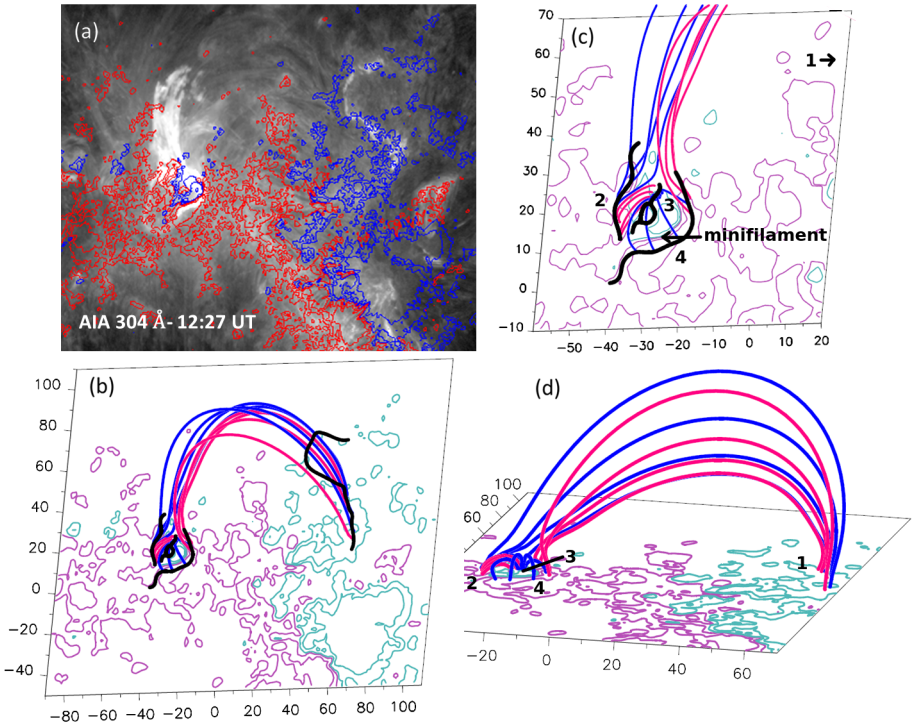

Figure 10 (**a**) AIA 304 image at 12:27 UT overlaid by HMI isocontours. The flare kernels at the bipole locations and the elongated far kernel on the western negative AR polarity (numbered *1*) are clearly visible. The EUV surge is observed to rise from eastern side of the bipoles. (**b**) Intersection of QSL traces (*black thick continuous lines*) with the photospheric plane for the same FOV as that shown in panel **a**. Two *sets* of field lines, representing the pre-reconnected (in *blue*) and reconnected field lines (in *red*) as inferred from the flare and surge evolution have been added (see also Figure 11). QSL traces match those of flare brightenings, and the shape of the *red* field lines approximately follows the trajectory of the EUV surge. (**c**) A zoom of the QSL traces in the neighborhood of the bipoles whose rotation and cancellation forced the mini-filament eruption and the initiation of the flare and EUV surge. An *arrow* points to the location of the mini-filament along the PIL of bipole B1. Panels **b** and **c** are shown from the observer's point of view. (**d**) A different point of view selected to better display the 3D structure of the field lines. The axes in panels **b**, **c**, and **d** are in Mm and the isocontours of the field in all panels correspond to $\pm$ 100 and 500 G in continuous *magenta* (*blue*) style for the positive (negative) values. The numbers *1*–*4* label the polarities that are mainly involved in the event and correspond to those in Figures 1 and 11 (see Section 3.4). The FOV of panel **c** does not include polarity *1*, which is far to the west, as indicated with the *arrow*.

same scale, we see that the QSL photospheric traces agree well with the flare brightenings, while the EUV surge is cospatial with the set of large-scale red field lines (see also the surge evolution in the movie surge-closeup.mp4). Figure 10c shows a closer view of the shape of the QSLs around the rotating bipoles, as well as the QSL trace on the negative polarity of bipole B1 (numbered 3). Moreover, when we compare panels a and b of Figure 10, the shape of the QSL trace far to the west matches the curved shape of the distant flare kernel, k1. Consequently, as in other analyzed examples, QSLs lie where flare kernels or other energy release manifestations are observed (see references at the beginning of this sub-section).

The distribution of the positive magnetic field around the negative polarity of B1 suggests the possibility that an associated coronal magnetic null-point might exist in the global AR magnetic field configuration (see, *e.g.*the topology computations in Mandrini *et al.*, 2014).

Furthermore, this is also the case for the almost circular shape of the QSLs and the observed brightening at the location of the rotating bipoles (see references in Section 1). We searched for a magnetic null-point in the model shown in Figure 9 and did not find one that could be linked to the flare and surge. The reason for the absence of a null-point might be that the negative B1 polarity is not completely surrounded by positive magnetic field (a negative extension is seen to the north of B1). However, no magnetic null-point and associated separatrices are needed in an observed configuration for energy release during an active event, as has been shown in many other examples (see references at the beginning of this section) or proposed in jet and/or surge models and simulations (see references in Section 1). QSLs with a finite thickness are a generalization of the infinitely thin separatrices. If a null-point is present, its separatices surfaces will be found where QSLs are the thinnest and embedded within them (see Masson *et al.*, 2009, 2017; Mandrini *et al.*, 2014).

Finally, we note that the much smaller circular shape of the central QSL on the negative polarity of B1 (Figure 10c) appears because of a parasitic positive polarity that is present for a few hours at that location (this is a real parasitic polarity and not the artifact created by energetic particles, as shown in Figure 5c). There is no flare brightening or activity related to this small polarity. We claim that this parasitic polarity is not related to the flare and surge studied in this article, and we do not show the field line connectivity associated with it.

3.3. Comparison of the Computed Topology to Observations

Panels b and d of Figure 10 show a set of field lines computed from both sides of the circular QSL. Considering the observed evolution (Figures 3 – 6), we have drawn in blue field lines that represent loops before reconnection, while field lines in red correspond to loops after reconnection. From the observation and model results, we conclude that the short blue field lines anchored at polarities labeled 3 and 4 above the PIL of B1 reconnect with the long blue field lines anchored at 1 and 2. A local zoom of the connectivities is shown in Figure 10c. The two sets of red field lines are the result of this interaction. The shorter set is anchored at 2 and 3, where we observe flare kernels k2 and k3 in Figures 3 – 6 at around 12:31 UT. The longer set follows the shape of the EUV surge material moving to the west. This set of field lines starts at polarity 4, where kernel k4 is located, and ends at polarity 1, where the distant flare kernel k1 lies (compare panels a and b; see also panel d, which shows a more favorable view point, where we have not included the QSLs for clarity).

Finally, the movie with a close-up view of the mini-filament eruption and surge (surge-closeup.mp4) shows that the plasma first moves up along the longer set of red field lines anchored at 1 and 4, and at the end of the movie, it flows back toward the footpoints of the same field lines. Although it is more difficult to see because the set of red field lines anchored at 2 and 3 is much shorter, a similar motion of the plasma along them is present. Finally, the field of view (FOV) of the movie does not include the far kernel on the main AR polarity labeled 1, but it is clearly observed in Figures 3 – 5 and in the respective movies HASTA.mp4 and AIA304.mp4.

3.4. Physical Processes Involved

We now discuss a possible scenario to explain the observed events by analyzing in detail the connectivity of field lines traced, starting integration at both sides of the QSLs. Since our connectivity analysis provides only a static view, to facilitate our discussion of the progression of the processes that occur from the beginning of the events analyzed in this article,

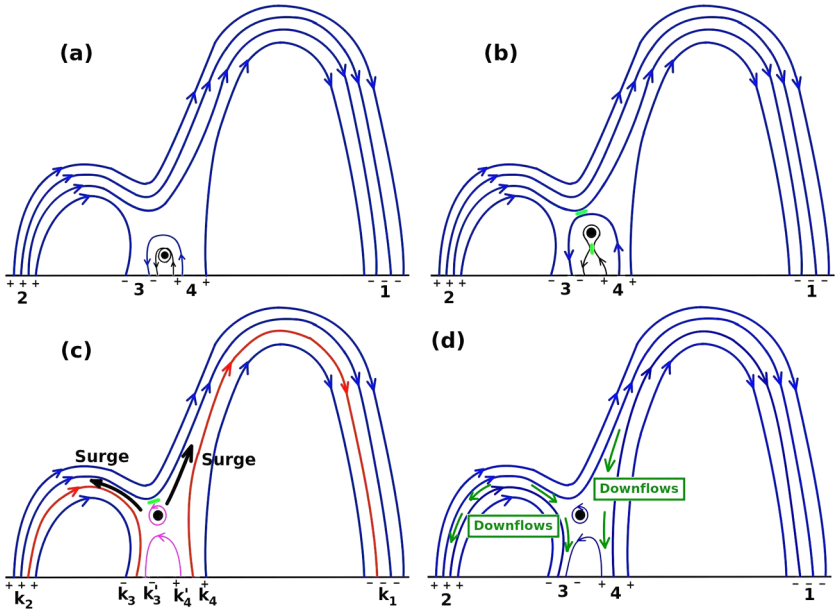

Figure 11 2D sketch illustrating the evolution of the flare and EUV surge. (**a**) *Sets* of *blue* magnetic field lines connecting polarities labeled *1 – 4*. The *small black circle* surrounded by a *black field line* represents the location of the mini-filament. This panel corresponds to the magnetic configuration before the eruption. (**b**) As the mini-filament erupts, two reconnection processes take place. Internal reconnection below the mini–filament, indicated with a *green short segment*, and external reconnection, also indicated with a *green segment* above the mini-filament. (**c**) The two reconnection processes at work. Internal reconnection transforms the *black field lines*, located around the mini-filament, in panel **b** into the *pink field lines* in this panel. The result of this internal reconnection process is the appearance of flare kernels k3′ and k4′. Simultaneously, external reconnection, between the *blue lines* connecting *3* and *4* and the *longer blue lines* connecting *1* and *2* in panel **b**, results in the *red field lines* connecting *2* with *3* and *1* with *4* indicated in this panel. The outcome of this second reconnection process is the injection of plasma forming the surge in the reconnected field lines. For a complete description of the two reconnection processes, see Section 3.4. (**d**) The downward flows are shown with *dark green arrows*. They occur later on in the previously reconnected field lines.

we include the schematic drawing shown in Figure 11. This sketch is similar to others proposed to explain jets (see, *e.g.* Sterling *et al.*, 2015, 2016; Joshi *et al.*, 2018; Moore, Sterling, and Panesar, 2018) in open field configurations; however, in our example, the background magnetic field is not open and unipolar, but closed and bipolar.

Panel a in Figure 11 corresponds to the situation before the flare and surge. The numbers at the base of the field lines label the magnetic polarities that are mainly involved in the events, as in Figure 1. The set of short blue field lines (anchored at 3 – 4) in Figure 11a overlies the mini-filament that is located along the PIL of B1, while the set of long blue field lines (anchored at 1 – 2) constitutes the background field, which is closed.

Due to a combination of flux cancellation along the B1 PIL and the bipole rotations, the mini-filament destabilizes and starts to rise (see Figure 11b). Magnetic reconnection sets in below the mini-filament (indicated with a short thick green segment) as in a classical prominence eruption (see *e.g.* Aulanier *et al.*, 2010; Webb and Howard, 2012). The pink lines in Figure 11c correspond to the reconnected field lines that result from this process, which has been called internal in several articles (see *e.g.* Sterling *et al.*, 2015; Moore, Sterling, and Panesar, 2018).

The short blue field lines that still restrain the mini-filament start to reconnect with the large-scale blue lines (see Figure 11b and c). This second reconnection process, indicated with a short thick green segment above the mini-filament, has been called external in the references listed before. The main difference with our particular case is that the configuration is closed.

In the case analyzed here, even if the magnetic tension above the mini-filament could decrease as some of the overlying field lines are transformed by reconnection in the red field lines at both sides, anchored at 2 – 3 and 1 – 4 in Figure 11c (see, *e.g.* Antiochos, DeVore, and Klimchuk, 1999), the plasma fails to reach farther out. As a result, it is injected into these red reconnected field lines. The material is seen to flow along them producing the surge (see Figure 11c). Finally, in Figure 11d we only indicate the direction of downflows along already reconnected lines as it occurs later on. To avoid an overly busy panel, we omit any reconnection process in this panel.

To summarize, the first internal reconnection process would yield the observed intense kernels at both sides of the PIL of B1, labeled k3′ and k4′ in Figure 4d and Figure 11c, and very short loops joining them. This location roughly corresponds to the place of the RHESSI contours that indicate the deposition of accelerated particles (Figure 5c). The second external reconnection process associated with kernels k1, k2, k3, and k4, observed in H_α and EUV (Figures 3 – 5) is captured by our global AR model and topology computation (Figure 10).

3.5. Comparison with Numerical Simulations

This observed case is similar to the results of the simulations of Wyper, Antiochos, and DeVore (2017) and Wyper, DeVore, and Antiochos (2018) (see also Pariat *et al.*, 2016, and references therein, although in these simulations no mini-filament is formed by the imposed twisting motions). In fact, both global magnetic configurations (ours and that in the simulations) are comparable with an embedded polarity within the dominant polarity of opposite sign. The driver in both cases is the shearing of the arcade below the magnetic dome, in contrast with other cases, where emergence is the dominant driver. Furthermore, in our observed case, magnetic flux cancellation also plays a role.

There are still several differences between our observations and the simulations. The main difference is that the observed central polarity is not fully surrounded by the opposite-sign polarity, which is possibly why no magnetic null is present in our extrapolation. From the QSL point of view, this does not imply a great difference since QSLs stay in place with a thickness that is very thin in comparison with MHD scales.

A second difference is the fully closed field configuration of our observations compared to the open field present in the simulations. Finally, the EUV surge is much less collimated than the jet found in the simulations. Except for these differences, the underlying physical mechanism is the same: magnetic reconnection of a sheared arcade where the mini-filament is embedded in a large-scale field.

3.6. Repetitive Events

All these processes started well before our analyzed example, as indicated by the fact that a surge and flare with similar characteristics occurred on 8 May (Section 2.4). The process of storage and release of magnetic energy is expected to continue for as long as the magnetic bipoles rotation and field cancellation persist. This evolution induces the reformation of a similar magnetic configuration, including the mini-filament.

Three surges and flares with similar characteristics occurred on 9 and 10 May after the surge we studied here. Of course, the location of QSLs in the region of the rotating bipoles would slightly change following their evolution, but the main characteristics are expected to be kept with a circular QSL and a distant one, since this topology is robust for as long as the negative polarity exists within the positive surrounding. The same repeating series of events was also found in some of the numerical simulations cited above (Pariat *et al.*, 2016, and references therein).

4. Conclusions

We analyzed the solar flare and confined ejection that occurred in NOAA AR 11476 on 9 May 2012. For the analysis we used magnetic, Hα, EUV, and soft and hard X-ray data from multiple space- and ground-based instruments (see Section 2). The way in which the plasma ejection developed is similar to the so-called blowout jets (see references in Section 1). The main difference is that in the event studied here, the material was ejected into closed magnetic field lines, while blowout jets usually occur (as regular jets do) along open magnetic structures. The velocity, angular span, and the fact that the ejection occurs in a closed magnetic structure recalls classical surges that are typically observed in Hα. However, it is also different from classical surges because a mini-filament, whose plasma forms part of the ejection, is present in the configuration. Furthermore, as we showed in Section 2, the Hα counterpart of the clearly observed ejection in AIA 304 and 171 is barely identifiable: Therefore we call this confined ejection an EUV surge. This is further confirmed by the thermal diagnostic analysis of Section 2.6, where we find that the surge material has its maximum emission at an approximate temperature of between 1.4 and 1.8×10^5 K, corresponding to the peak response of the AIA 304 channel.

By studying the evolution of the AR photospheric magnetic field during three days around the event, we identified two rotating bipoles in the central part of the main positive (following) polarity of the AR that coincide in location with the flare and surge ejection. The magnetic flux of these bipoles decreased steeply during the period when the rotation is observed. A mini-filament was seen lying along the PIL of the largest rotating bipole. We conclude that the sustained rotation of the bipoles is the main source of helicity and free magnetic energy accumulation that is later released during the events.

We estimate a northward surge velocity of 90 $\mathrm{km\,s^{-1}}$ in the plane of the sky as seen from Earth, which is consistent with the velocity estimate of 120 $\mathrm{km\,s^{-1}}$ as observed from the STEREO-B point of view (see Sections 2.4 and 2.5). These are typical velocity values observed in previously studied jets and surges (see Section 1). We also identify a torsional component in the development of the ejection, which is very likely associated with the magnetic helicity injected during the rotation of the bipoles.

As in several recent observations of coronal jets, a mini-filament is present along the PIL of the main rotating bipole. We propose that its rotation, combined with flux cancellation, destabilizes the mini-filament and brings it to eruption. Magnetic reconnection below the mini-filament, called internal reconnection, is mainly responsible for the brightest flare kernels and particle acceleration whose deposition sites are seen as elongated RHESSI contours. Simultaneously, external magnetic reconnection occurs between the loops within which the erupting mini-filament is embedded and the closed AR loops forming the background field. This reconnection is at the origin of four flare kernels. Two are located on the main rotating bipole, while the other two are located on the AR polarities.

Next, we combined the observations with coronal magnetic field extrapolations using HMI magnetograms as boundary condition (Section 3.1). Our global magnetic field model lets us explain the external reconnection process that occur as the mini-filament and its field configuration are destabilized and erupt. We determined the location of the QSL traces at the photospheric level and related them to the observed location of flare kernels (Section 3.4). In particular, the shapes and locations of QSL traces consist of an almost circular QSL surrounding most of the two rotating bipoles plus an elongated QSL on the main AR negative polarity to the west (see Figure 10). The circular QSL trace coincides with the flare kernels observed both in Hα and EUV, while the elongated trace corresponds to a far flare kernel (Section 3.4).

Furthermore, a continuous faint brightening at the location of the circular QSL is observable about a day before our analyzed event, showing that the above topology was present long before. We argue that the sustained bipole rotations (≈ 72 hr) allows for magnetic helicity and energy storage among at least five flare and surge events (one on 8 May and two on both 9 and 10 May) and also, most probably, contributes to the reformation of the mini-filament. We find that the timescale of energy storage (with slow reconnection involved) is between 7 and 23 hours, with a mean of about 14 hours.

Going deeper in the analysis, we selected as a starting integration points both sides of the computed QSLs to compute sets of magnetic field lines with different connectivities and reconstructed the spatial evolution of the event, which allowed us to determine the role of the different loop structures. The computed connectivities confirm the above interpretation, as summarized in Figure 10. This allowed us to derive a detailed scenario of the physics involved (Figure 11).

It is remarkable in the events analyzed here that contrary to what has been proposed in numerical jet and surge simulations (see references in the Section 1), the surge and flare do not seem to have been driven by magnetic flux emergence. This has also been shown to be the case in other jet observations (see *e.g.* Adams *et al.*, 2014; Panesar, Sterling, and Moore, 2016; Joshi *et al.*, 2018). The magnetic flux measurements indicate that the bipoles (mainly B1) are in decay, strongly suggesting that the main driver is the shearing of the arcade and flux cancellation within bipole B1.

This observed example is similar to the results of the simulations by Wyper, Antiochos, and DeVore (2017) and Wyper, DeVore, and Antiochos (2018) (see also, Pariat *et al.*, 2016, and references therein). The magnetic configurations, observed in our case and simulated in the previous articles, are comparable, since both have an embedded polarity within a dominant polarity of opposite sign. The driver in both cases is due to the shearing of an arcade, with flux cancellation also playing a role in the filament destabilization. A difference is that our configuration is formed by closed field lines compared to the open field in the simulations, and furthermore, the EUV surge is less collimated than the jet found in the numerical model.

Finally, the global AR magnetic field structure analyzed here lets us conclude that no magnetic null-point and associated separatrices are needed in an observed configuration for energy release, as has been shown in many other examples (see references in Section 3.2). QSLs with a finite thickness are a generalization of the infinitely thin separatrices. If a null-point is present, its separatices are located where QSLs are the thinnest and embedded within them (see Masson *et al.*, 2009, 2017; Mandrini *et al.*, 2014).

Acknowledgements The authors are grateful for the insightful referee, who stimulated us to improve several parts of the manuscript. The authors would like to thank Carlos Francile from the Astronomical Observatory Felix Aguilar, University of San Juan, for his invaluable help in the processing of HASTA data. MLF,

CHM and GC are members of the Carrera del Investigador Científico of the Consejo Nacional de Investigaciones Científicas y Técnicas (CONICET) of Argentina. MP and FL are CONICET Fellows. MP, MLF, GC and CHM acknowledge financial support from the Argentinean grants PICT 2012-0973 (ANPCyT), UBACyT 20020130100321 and PIP 2012-01-403 (CONICET).

Disclosure of Potential Conflicts of Interest The authors declare that they have no conflicts of interest.

References

Adams, M., Sterling, A.C., Moore, R.L., Gary, G.A.: 2014, A small-scale eruption leading to a blowout macrospicule jet in an on-disk coronal hole. *Astrophys. J.* **783**, 11. DOI. ADS.

Alissandrakis, C.E.: 1981, On the computation of constant alpha force-free magnetic field. *Astron. Astrophys.* **100**, 197. ADS.

Antiochos, S.K., DeVore, C.R., Klimchuk, J.A.: 1999, A model for solar coronal mass ejections. *Astrophys. J.* **510**, 485. DOI. ADS.

Aulanier, G., Pariat, E., Démoulin, P.: 2005, Current sheet formation in quasi-separatrix layers and hyperbolic flux tubes. *Astron. Astrophys.* **444**, 961. DOI. ADS.

Aulanier, G., Török, T., Démoulin, P., DeLuca, E.E.: 2010, Formation of torus-unstable flux ropes and electric currents in erupting sigmoids. *Astrophys. J.* **708**, 314. DOI. ADS.

Bagalá, L.G., Bauer, O.H., Fernández Borda, R., Francile, C., Haerendel, G., Rieger, R., Rovira, M.G.: 1999, The new Hα solar telescope at the German–Argentinian solar observatory. In: Wilson, A., *et al.* (eds.) *Magnetic Fields and Solar Processes*, *ESA Special Publication* **448**, 469. ADS.

Bagalá, L.G., Mandrini, C.H., Rovira, M.G., Démoulin, P.: 2000, Magnetic reconnection: a common origin for flares and AR interconnecting arcs. *Astron. Astrophys.* **363**, 779. ADS.

Brooks, D.H., Kurokawa, H., Berger, T.E.: 2007, An Hα surge provoked by moving magnetic features near an emerging flux region. *Astrophys. J.* **656**, 1197. DOI. ADS.

Büchner, J.: 2006, Locating current sheets in the solar corona. *Space Sci. Rev.* **122**, 149. DOI. ADS.

Canfield, R.C., Reardon, K.P., Leka, K.D., Shibata, K., Yokoyama, T., Shimojo, M.: 1996, H alpha surges and X-ray jets in AR 7260. *Astrophys. J.* **464**, 1016. DOI. ADS.

Chae, J., Qiu, J., Wang, H., Goode, P.R.: 1999, Extreme-ultraviolet jets and Hα surges in solar microflares. *Astrophys. J. Lett.* **513**, L75. DOI. ADS.

Chandra, R., Mandrini, C.H., Schmieder, B., Joshi, B., Cristiani, G.D., Cremades, H., Pariat, E., Nuevo, F.A., Srivastava, A.K., Uddin, W.: 2017, Blowout jets and impulsive eruptive flares in a bald-patch topology. *Astron. Astrophys.* **598**, A41. DOI. ADS.

Cristiani, G., Martinez, G., Mandrini, C.H., Giménez de Castro, C.G., da Silva, C.W., Rovira, M.G., Kaufmann, P.: 2007, Spatial characterization of a flare using radio observations and magnetic field topology. *Solar Phys.* **240**, 271. DOI. ADS.

Démoulin, P.: 2006, Extending the concept of separatrices to QSLs for magnetic reconnection. *Adv. Space Res.* **37**, 1269. DOI. ADS.

Démoulin, P., Hénoux, J.C., Priest, E.R., Mandrini, C.H.: 1996, Quasi-separatrix layers in solar flares. I. Method. *Astron. Astrophys.* **308**, 643. ADS.

Démoulin, P., Bagalá, L.G., Mandrini, C.H., Hénoux, J.C., Rovira, M.G.: 1997, Quasi-separatrix layers in solar flares. II. Observed magnetic configurations. *Astron. Astrophys.* **325**, 305. ADS.

Effenberger, F., Thust, K., Arnold, L., Grauer, R., Dreher, J.: 2011, Numerical simulation of current sheet formation in a quasi-separatrix layer using adaptive mesh refinement. *Phys. Plasmas* **18**, 32902.

Fernandez Borda, R.A., Mininni, P.D., Mandrini, C.H., Gómez, D.O., Bauer, O.H., Rovira, M.G.: 2002, Automatic solar flare detection using neural network techniques. *Solar Phys.* **206**, 347. DOI. ADS.

Foukal, P.V.: 2004, *Solar Astrophysics*, 2nd edn., 480. ADS.

Golub, L., Deluca, E., Austin, G., Bookbinder, J., Caldwell, D., Cheimets, P., *et al.*: 2007, The X-Ray Telescope (XRT) for the Hinode mission. *Solar Phys.* **243**, 63. DOI. ADS.

Green, L.M., López fuentes, M.C., Mandrini, C.H., Démoulin, P., Van Driel-Gesztelyi, L., Culhane, J.L.: 2002, The magnetic helicity budget of a cme-prolific active region. *Solar Phys.* **208**, 43. DOI. ADS.

Guglielmino, S.L., Bellot Rubio, L.R., Zuccarello, F., Aulanier, G., Vargas Domínguez, S., Kamio, S.: 2010, Multiwavelength observations of small-scale reconnection events triggered by magnetic flux emergence in the solar atmosphere. *Astrophys. J.* **724**, 1083. DOI. ADS.

Guo, Y., Démoulin, P., Schmieder, B., Ding, M.D., Vargas Domínguez, S., Liu, Y.: 2013, Recurrent coronal jets induced by repetitively accumulated electric currents. *Astron. Astrophys.* **555**, A19. DOI. ADS.

Harrison, R.A., Sime, D.G., Pearce, G.: 1990, The surge events of June 28 and October 30, 1980. *Astron. Astrophys.* **238**, 347. ADS.

Heyvaerts, J., Priest, E., Rust, D.M.: 1977, An emerging flux model for solar flares. *Solar Phys.* **53**, 255. DOI. ADS.

Howard, R.A., Moses, J.D., Vourlidas, A., Newmark, J.S., Socker, D.G., Plunkett, S.P., *et al.*: 2008, Sun Earth connection coronal and heliospheric investigation (SECCHI). *Space Sci. Rev.* **136**, 67. DOI. ADS.

Janvier, M., Aulanier, G., Pariat, E., Démoulin, P.: 2013, The standard flare model in three dimensions. III. Slip-running reconnection properties. *Astron. Astrophys.* **555**, A77. DOI. ADS.

Janvier, M., Savcheva, A., Pariat, E., Tassev, S., Millholland, S., Bommier, V., McCauley, P., McKillop, S., Dougan, F.: 2016, Evolution of flare ribbons, electric currents, and quasi-separatrix layers during an X-class flare. *Astron. Astrophys.* **591**, A141. DOI. ADS.

Jibben, P., Canfield, R.C.: 2004, Twist propagation in Hα surges. *Astrophys. J.* **610**, 1129. DOI. ADS.

Joshi, N.C., Liu, C., Sun, X., Wang, H., Magara, T., Moon, Y.-J.: 2015, The role of erupting sigmoid in triggering a flare with parallel and large-scale quasi-circular ribbons. *Astrophys. J.* **812**, 50. DOI. ADS.

Joshi, N.C., Sterling, A.C., Moore, R.L., Magara, T., Moon, Y.-J.: 2017, Onset of a large ejective solar eruption from a typical coronal-jet-base field configuration. *Astrophys. J.* **845**, 26. DOI. ADS.

Joshi, N.C., Nishizuka, N., Filippov, B., Magara, T., Tlatov, A.G.: 2018, Flux rope breaking and formation of a rotating blowout jet. *Mon. Not. Roy. Astron. Soc.* **476**, 1286. DOI. ADS.

Karpen, J.T., Antiochos, S.K., DeVore, C.R.: 2012, The mechanisms for the onset and explosive eruption of coronal mass ejections and eruptive flares. *Astrophys. J.* **760**, 81. DOI. ADS.

Lemen, J.R., Title, A.M., Akin, D.J., Boerner, P.F., Chou, C., Drake, J.F., *et al.*: 2012, The atmospheric imaging assembly (AIA) on the solar dynamics observatory (SDO). *Solar Phys.* **275**, 17. DOI. ADS.

Li, H., Yang, J., Jiang, Y., Bi, Y., Qu, Z., Chen, H.: 2018, The surge-like eruption of a miniature filament associated with circular flare ribbon. *Astrophys. Space Sci.* **363**, 26. DOI. ADS.

Lin, R.P., Dennis, B.R., Hurford, G.J., Smith, D.M., Zehnder, A., Harvey, P.R., *et al.*: 2002, The Reuven Ramaty High-Energy Solar Spectroscopic Imager (RHESSI). *Solar Phys.* **210**, 3. DOI. ADS.

Liu, Y., Kurokawa, H.: 2004, On a surge: properties of an emerging flux region. *Astrophys. J.* **610**, 1136. DOI. ADS.

Liu, C., Deng, N., Liu, R., Ugarte-Urra, I., Wang, S., Wang, H.: 2011, A standard-to-blowout jet. *Astrophys. J. Lett.* **735**, L18. DOI. ADS.

Longcope, D.W.: 2005, Topological methods for the analysis of solar magnetic fields. *Living Rev. Solar Phys.* **2**, 7. DOI. ADS.

López Fuentes, M.C., Klimchuk, J.A., Mandrini, C.H.: 2007, The temporal evolution of coronal loops observed by GOES SXI. *Astrophys. J.* **657**, 1127. DOI. ADS.

López Fuentes, M.C., Poisson, M., Mandrini, C.H., Luoni, M.L., Cristiani, G.D., Démoulin, P.: 2015, Análisis de un evento eyectivo en una arcada cerrada. In: *CRAAA* **58**, 37. http://www.astronomiaargentina.org.ar/uploads/docs/craaa58.pdf.

MacTaggart, D., Guglielmino, S.L., Haynes, A.L., Simitev, R., Zuccarello, F.: 2015, The magnetic structure of surges in small-scale emerging flux regions. *Astron. Astrophys.* **576**, A4. DOI. ADS.

Mandrini, C.H.: 2010, Magnetic energy release: flares and coronal mass ejections. In: Kosovichev, A.G., Andrei, A.H., Rozelot, J.-P. (eds.) *IAU Symposium* **264**, 257. DOI. ADS.

Mandrini, C.H., Démoulin, P., van Driel-Gesztelyi, L., Schmieder, B., Cauzzi, G., Hofmann, A.: 1996, 3D magnetic reconnection at an X-ray bright point. *Solar Phys.* **168**, 115. DOI. ADS.

Mandrini, C.H., Démoulin, P., Schmieder, B., Deng, Y.Y., Rudawy, P.: 2002, The role of magnetic bald patches in surges and arch filament systems. *Astron. Astrophys.* **391**, 317. DOI. ADS.

Mandrini, C.H., Demoulin, P., Schmieder, B., Deluca, E.E., Pariat, E., Uddin, W.: 2006, Companion event and precursor of the X17 flare on 28 October 2003. *Solar Phys.* **238**, 293. DOI. ADS.

Mandrini, C.H., Schmieder, B., Démoulin, P., Guo, Y., Cristiani, G.D.: 2014, Topological analysis of emerging bipole clusters producing violent solar events. *Solar Phys.* **289**, 2041. DOI. ADS.

Mandrini, C.H., Baker, D., Démoulin, P., Cristiani, G.D., van Driel-Gesztelyi, L., Vargas Domínguez, S., Nuevo, F.A., Vásquez, A.M., Pick, M.: 2015, Parallel evolution of quasi-separatrix layers and active region upflows. *Astrophys. J.* **809**, 73. DOI. ADS.

Masson, S., Pariat, E., Aulanier, G., Schrijver, C.J.: 2009, The nature of flare ribbons in coronal null-point topology. *Astrophys. J.* **700**, 559. DOI. ADS.

Masson, S., Aulanier, G., Pariat, E., Klein, K.-L.: 2012, Interchange slip-running reconnection and sweeping SEP beams. *Solar Phys.* **276**, 199. DOI. ADS.

Masson, S., Pariat, É., Valori, G., Deng, N., Liu, C., Wang, H., Reid, H.: 2017, Flux rope, hyperbolic flux tube, and late extreme ultraviolet phases in a non-eruptive circular-ribbon flare. *Astron. Astrophys.* **604**, A76. DOI. ADS.

Milano, L.J., Dmitruk, P., Mandrini, C.H., Gómez, D.O., Démoulin, P.: 1999, Quasi-separatrix layers in a reduced magnetohydrodynamic model of a coronal loop. *Astrophys. J.* **521**, 889.

Moore, R.L., Sterling, A.C., Panesar, N.K.: 2018, Onset of the magnetic explosion in solar polar coronal X-ray jets. *Astrophys. J.* **859**, 3. DOI. ADS.

Moore, R.L., Cirtain, J.W., Sterling, A.C., Falconer, D.A.: 2010, Dichotomy of solar coronal jets: standard jets and blowout jets. *Astrophys. J.* **720**, 757. DOI. ADS.

Moreno-Insertis, F., Galsgaard, K.: 2013, Plasma jets and eruptions in solar coronal holes: a three-dimensional flux emergence experiment. *Astrophys. J.* **771**, 20. DOI. ADS.

Nóbrega-Siverio, D., Moreno-Insertis, F., Martínez-Sykora, J.: 2016, The cool surge following flux emergence in a radiation-MHD experiment. *Astrophys. J.* **822**, 18. DOI. ADS.

Panesar, N.K., Sterling, A.C., Moore, R.L.: 2016, Homologous jet-driven coronal mass ejections from solar active region 12192. *Astrophys. J. Lett.* **822**, L23. DOI. ADS.

Panesar, N.K., Sterling, A.C., Moore, R.L., Chakrapani, P.: 2016, Magnetic flux cancelation as the trigger of solar quiet-region coronal jets. *Astrophys. J. Lett.* **832**, L7. DOI. ADS.

Pariat, E., Antiochos, S.K., DeVore, C.R.: 2009, A model for solar polar jets. *Astrophys. J.* **691**, 61. DOI. ADS.

Pariat, E., Antiochos, S.K., DeVore, C.R.: 2010, Three-dimensional modeling of quasi-homologous solar jets. *Astrophys. J.* **714**, 1762. DOI. ADS.

Pariat, E., Aulanier, G., Démoulin, P.: 2006, A new concept for magnetic reconnection : slip-running reconnection. In: Barret, D., Casoli, F., Lagache, G., Lecavelier, A., Pagani, L. (eds.) *SF2A-2006: Semaine de L'Astrophysique Francaise*, 559. ADS.

Pariat, E., Dalmasse, K., DeVore, C.R., Antiochos, S.K., Karpen, J.T.: 2015, Model for straight and helical solar jets. I. Parametric studies of the magnetic field geometry. *Astron. Astrophys.* **573**, A130. DOI. ADS.

Pariat, E., Dalmasse, K., DeVore, C.R., Antiochos, S.K., Karpen, J.T.: 2016, A model for straight and helical solar jets. II. Parametric study of the plasma beta. *Astron. Astrophys.* **596**, A36. DOI. ADS.

Poisson, M., Mandrini, C.H., Démoulin, P., López Fuentes, M.: 2015, Evidence of twisted flux-tube emergence in active regions. *Solar Phys.* **290**, 727. DOI. ADS.

Poisson, M., Démoulin, P., López Fuentes, M., Mandrini, C.H.: 2016, Properties of magnetic tongues over a solar cycle. *Solar Phys.* **291**, 1625. DOI. ADS.

Polito, V., Del Zanna, G., Valori, G., Pariat, E., Mason, H.E., Dudík, J., Janvier, M.: 2017, Analysis and modelling of recurrent solar flares observed with Hinode/EIS on March 9, 2012. *Astron. Astrophys.* **601**, A39. DOI. ADS.

Qiu, J., Gary, D.E.: 2003, Flare-related magnetic anomaly with a sign reversal. *Astrophys. J.* **599**, 615. DOI. ADS.

Raouafi, N.E., Patsourakos, S., Pariat, E., Young, P.R., Sterling, A.C., Savcheva, A., Shimojo, M., Moreno-Insertis, F., DeVore, C.R., Archontis, V., Török, T., Mason, H., Curdt, W., Meyer, K., Dalmasse, K., Matsui, Y.: 2016, Solar coronal jets: observations, theory, and modeling. *Space Sci. Rev.* **201**, 1. DOI. ADS.

Roy, J.R.: 1973, The magnetic properties of solar surges. *Solar Phys.* **28**, 95. DOI. ADS.

Rust, D.M., Hildner, E., Hansen, R.T., Dryer, M., McClymont, A.N., McKenna-Lawlor, S.M.P., McLean, D.J., Schmahl, E.J., Steinolfson, R.S., Tandberg-Hanssen, E.: 1980, Mass ejections. In: Sturrock, P.A. (ed.) *Skylab Solar Workshop II*, 273. ADS.

Savcheva, A.S., van Ballegooijen, A.A., DeLuca, E.E.: 2012, Field topology analysis of a long-lasting coronal sigmoid. *Astrophys. J.* **744**, 78. DOI. ADS.

Savcheva, A., Pariat, E., McKillop, S., McCauley, P., Hanson, E., Su, Y., Werner, E., DeLuca, E.E.: 2015, The relation between solar eruption topologies and observed flare features. I. Flare ribbons. *Astrophys. J.* **810**, 96. DOI. ADS.

Scherrer, P.H., Schou, J., Bush, R.I., Kosovichev, A.G., Bogart, R.S., Hoeksema, J.T., *et al.*: 2012, The Helioseismic and Magnetic Imager (HMI) investigation for the Solar Dynamics Observatory (SDO). *Solar Phys.* **275**, 207. DOI. ADS.

Schmahl, E.J.: 1981, The physical relationship between flares and surges observed in the extreme ultraviolet. *Solar Phys.* **69**, 135. DOI. ADS.

Schmieder, B., Mein, P., Simnett, G.M., Tandberg-Hanssen, E.: 1988, An example of the association of X-ray and UV emission with H-alpha surges. *Astron. Astrophys.* **201**, 327. ADS.

Schmieder, B., Shibata, K., van Driel-Gesztelyi, L., Freeland, S.: 1995, H alpha surges and associated soft X-ray loops. *Solar Phys.* **156**, 245. DOI. ADS.

Shen, Y., Liu, Y., Su, J., Deng, Y.: 2012, On a coronal blowout jet: the first observation of a simultaneously produced bubble-like CME and a jet-like CME in a solar event. *Astrophys. J.* **745**, 164. DOI. ADS.

Shibata, K., Ishido, Y., Acton, L.W., Strong, K.T., Hirayama, T., Uchida, Y., *et al.*: 1992, Observations of X-ray jets with the YOHKOH soft X-ray telescope. *Publ. Astron. Soc. Japan* **44**, L173. ADS.

Sterling, A.C., Moore, R.L., Falconer, D.A., Adams, M.: 2015, Small-scale filament eruptions as the driver of X-ray jets in solar coronal holes. *Nature* **523**, 437. DOI. ADS.

Sterling, A.C., Moore, R.L., Falconer, D.A., Panesar, N.K., Akiyama, S., Yashiro, S., Gopalswamy, N.: 2016, Minifilament eruptions that drive coronal jets in a solar active region. *Astrophys. J.* **821**, 100. DOI. ADS.

Titov, V.S., Hornig, G., Démoulin, P.: 2002, Theory of magnetic connectivity in the solar corona. *J. Geophys. Res.* **107**, 1164.

Uddin, W., Schmieder, B., Chandra, R., Srivastava, A.K., Kumar, P., Bisht, S.: 2012, Observations of multiple surges associated with magnetic activities in AR 10484 on 2003 October 25. *Astrophys. J.* **752**, 70. DOI. ADS.

Vargas Domínguez, S., Kosovichev, A., Yurchyshyn, V.: 2014, Multi-wavelength high-resolution observations of a small-scale emerging magnetic flux event and the chromospheric and coronal response. *Astrophys. J.* **794**, 140. DOI. ADS.

Webb, D.F., Howard, T.A.: 2012, Coronal mass ejections: observations. *Living Rev. Solar Phys.* **9**, 3. DOI. ADS.

Wilmot-Smith, A.L., Hornig, G., Pontin, D.I.: 2009, Magnetic braiding and parallel electric fields. *Astrophys. J.* **696**, 1339.

Wyper, P.F., Antiochos, S.K., DeVore, C.R.: 2017, A universal model for solar eruptions. *Nature* **544**, 452. DOI. ADS.

Wyper, P.F., DeVore, C.R., Antiochos, S.K.: 2018, A breakout model for solar coronal jets with filaments. *Astrophys. J.* **852**, 98. DOI. ADS.

Yang, S., Zhang, J.: 2018, Mini-filament eruptions triggering confined solar flares observed by ONSET and SDO. *Astrophys. J. Lett.* **860**, L25. DOI. ADS.

Yokoyama, T., Shibata, K.: 1995, Magnetic reconnection as the origin of X-ray jets and Hα surges on the Sun. *Nature* **375**, 42. DOI. ADS.

Yokoyama, T., Shibata, K.: 1996, MHD simulation of solar coronal X-ray jets: emerging flux reconnection model. *Astrophys. Lett. Commun.* **34**, 133. ADS.

Young, P.R., Muglach, K.: 2014a, A coronal hole jet observed with Hinode and the solar dynamics observatory. *Publ. Astron. Soc. Japan* **66**, S12. DOI. ADS.

Young, P.R., Muglach, K.: 2014b, Solar dynamics observatory and Hinode observations of a blowout jet in a coronal hole. *Solar Phys.* **289**, 3313. DOI. ADS.

Zhao, J., Li, H., Pariat, E., Schmieder, B., Guo, Y., Wiegelmann, T.: 2014, Temporal evolution of the magnetic topology of the NOAA active region 11158. *Astrophys. J.* **787**, 88. DOI. ADS.